frontiers in Earth Science

ORIGINAL RESEARCH
published: 25 August 2020
doi: 10.3389/feart.2020.00357

Mineralogical and Geochemical Study on the Yaojiazhuang Ultrapotassic Complex, North China Craton: Constraints on the Magmatic Differentiation Processes and Genesis of Apatite Ores

Ronghao Pan, Tong Hou and Zhaochong Zhang*

State Key Laboratory of Geological Process and Mineral Resources, China University of Geosciences, Beijing, China

The differentiation process of ultrapotassic magmas is enigmatic and poorly understood. The Yaojiazhuang ultrapotassic complex is concentrically zoned by late-intruded syenite in the core and early emplaced clinopyroxenite in the periphery, combining a "bi-modal" lithology. Spatially, apatite and iron oxide-apatite (IOA) ores, glimmerite and pseudoleucite occur in the upper part of clinopyroxenite. The syenite and clinopyroxenite are composed of variable amounts of clinopyroxenite, biotite, K-feldspar, magnetite, apatite with minor analcite, titanite, and primary calcite. The pseudoleucite clinopyroxenite contains mainly clinopyroxene, biotite and garnet in the matrix, and nepheline–K-feldspar intergrowth with muscovite and minor celestine in the leucite pseudomorph. Geochemically, rocks of the Yaojiazhuang complex are significantly enriched in potassium (K), light rare earth elements (LREE), and large ion lithophile elements (LILE). Crustal contamination by Archean tonalite–trondhjemite–granodiorite (TTG) gneisses basement may play an important role to convert the syenitic melts from silica-undersaturation to saturation. Fractionation crystallization is supported by the mineral crystallization sequence to explain the bimodal lithologies instead of silicate liquid immiscibility. During the magmatic evolution, decompression, fractionation of volatile-poor clinopyroxene and the enhancement by CO_2 may result in the exsolution of an aqueous fluid. The late-stage interactions between existing minerals and magmatic fluids in the crystal mush could be a key process in the generation of both leucite pseudomorphs and apatite/IOA ores.

Keywords: ultrapotassic, Yaojiazhuang complex, fluid exsolution, apatite, pseudoleucite, syenite, clinopyroxenite, North China Craton

OPEN ACCESS

Edited by:
David R. Lentz,
University of New Brunswick, Canada

Reviewed by:
Wei Chen,
China University of Geosciences, China
Jinyang Zhang,
China University of Geosciences, China

****Correspondence:***
Tong Hou
thou@cugb.edu.cn

Specialty section:
This article was submitted to Economic Geology, a section of the journal Frontiers in Earth Science

Received: *10 April 2020*
Accepted: *31 July 2020*
Published: *25 August 2020*

Citation:
Pan R, Hou T and Zhang Z (2020) Mineralogical and Geochemical Study on the Yaojiazhuang Ultrapotassic Complex, North China Craton: Constraints on the Magmatic Differentiation Processes and Genesis of Apatite Ores. Front. Earth Sci. 8:357. doi: 10.3389/feart.2020.00357

INTRODUCTION

The occurrence of ultrapotassic rocks is volumetrically rare, with the origin usually related to intraplate extension environments and collision zones (e.g., Foley et al., 1987; Miller et al., 1999; Conticelli et al., 2007, 2009, 2013). Considerable amounts of studies had been conducted on ultrapotassic rocks which are mostly focusing on their mantle source and partial melting

processes (e.g., Thompson et al., 1990; Conticelli and Peccerillo, 1992; Foley and Peccerillo, 1992; Rogers et al., 1992; Zhang et al., 1995; Miller et al., 1999; Lobach-Zhuchenko et al., 2008; Gaeta et al., 2016). Metasomatized mantle sources and relatively low degree of melting process had been proposed for the generation of ultrapotassic primary melts (e.g., Dawson, 1987; Marks et al., 2008; Sun et al., 2014; Bodeving et al., 2017; Soder and Romer, 2018; Sokół et al., 2018). Nevertheless, most of the ultrapotassic rocks are not solidified from primary mantle-derived liquids, thus the subsequent differentiation processes of ultrapotassic magmas in the crust including fractionation crystallization, crustal contamination, magma (un-)mixing and mingling, and exsolution/transportation of both magmatic and post-magmatic fluids could also play important roles in the formation of them (e.g., Ferlito and Lanzafame, 2010; Jeffery et al., 2013; Brenna et al., 2015; Wolff, 2017; Burchardt, 2018). However, to the best of our knowledge, these crustal processes are poorly constrained. Hence, a comprehensive illustration on the differentiation processes is crucial for our understanding about the formation of ultrapotassic rocks.

Moreover, some alkaline rocks, including ultrapotassic rocks are associated with mineral deposits, mainly apatite ± magnetite ± minor silicate minerals (phoscorite, IOA ores and monomineralic apatite ores), such as Ordovician-Silurian Misvaerdal complex in Norway (Ihlen et al., 2014), Khibiny complex in Kola Peninsula, Russia (Notholt, 1979; Kogarko, 2018) and Mushgai-Khudag Complex, South Mongolia (Nikolenko et al., 2018). Accordingly, the formation of these P-rich ores is genetically related to the differentiation of the alkaline magmas. Two major models including fractional crystallization (Hou et al., 2015) and liquid immiscibility (Kolker, 1982; Jiang et al., 2004; Mokhtari et al., 2013) had been proposed for the formation of these apatite and IOA ores. Therefore, it is of great significance to elucidate the petrogenesis of ore-bearing alkaline complex, which could potentially shed new lights on the formation of the apatite and IOA ores.

The Yaojiazhuang alkaline plutonic intrusion is a "bi-modal" ring complex with syenite in the core and clinopyroxenite in the periphery generated by ultrapotassic magmas frozen in the crust according to previous studies (Chen et al., 2013). Notably, there is also a large apatite and IOA ore deposit hosted at the upper part of clinopyroxenite and have been mined as phosphorus deposit for decades. However, the formation mechanism of bi-modal lithofacies and tons of phosphorus concentration are still in widely debates and remain poorly understood (e.g., Hou, 1990b; Mu and Yan, 1992; Zhang, 1999; Chen et al., 2013; Tang et al., 2014; Liu and Tang, 2018). Previous studies suggested that the compositionally contrasting syenite and clinopyroxenite could be the Si-rich and Fe-rich melts produced by silicate liquid immiscibility from a common ultrapotassic parental magma, supported by thermodynamic simulations (Hou, 1990b; Ma et al., 1999), and during the separation of immiscible liquids, P_2O_5 tends to be partitioned into the Fe-rich melts and thus form the apatite and IOA ore in clinopyroxenite (Hou, 1990a). Alternatively, other authors commonly favor fractional crystallization either for Yaojiazhuang complex (Chen et al., 2013) or adjacent Fanshan complex (Cheng and Sun, 2003; Hou et al., 2015).

Additionally, the widespread hydrated minerals like biotite and the occurrence of pegmatites which has not been reported in detail indicate that during the formation of Yaojiazhuang complex, the magma ought to be enriched in fluids. Recent studies had revealed that the interactions between fluids and minerals during the last magmatic stage could significantly modify rock structures and textures, and could also act as a key mechanism in the generation of economic ore deposits, especially apatite and IOA deposits (e.g., Roedder, 1992; Huber et al., 2012; Ballhaus et al., 2015; Guo and Audétat, 2017; La Cruz et al., 2019; Knipping et al., 2019). Therefore, a combined study involving mineralogy, petrology and geochemistry studies is required to elucidate these processes. Thus in this paper, we conducted comprehensive study for the differentiation of Yaojiazhuang complex, in order to better understand the differentiation processes of ultrapotassic magmas and shed new lights on the formation of the apatite and IOA ores.

GEOLOGICAL SETTING

Regional Geology

The Yaojiazhuang ultrapotassic complex is located at the north margin of the North China Craton (NCC), ∼160 km northwest of the Beijing city (**Figure 1A**). The basement rocks of NCC are mainly mafic granulites, amphibolites and tonalite–trondhjemite–granodiorite (TTG) gneisses of ages up to 3.85 Ga (Liu et al., 1992), and are overlain unconformably by Meso- to Neo-Proterozoic sediments (Zhao et al., 2001). To the north of the NCC is the Central Asian Orogenic Belt, which strongly influenced the northern margin of NCC during Carboniferous to Permian by the progressive closure of Paleo-Asian Ocean leading to Andean-type magmatism and Himalayan-type collision, and formation of the Solonker suture (e.g., Xiao et al., 2003; Zhang et al., 2009). Following the closure was a post-collisional extension during early Mesozoic, resulting in a series of magmatic emplacement events and forming a > 1,500 km E-W trending alkaline rock belt along the northern margin of NCC (e.g., Zhang and Wang, 1997; Zhang, 1999; Zhao et al., 2008; Ren et al., 2009; Zhang et al., 2012). The major rock types can be divided mainly into three associations: (1) clinopyroxene diorite – quartz syenite – aegirine syenite – syenite – granite association, such as Shuiquangou complex; (2) nepheline syenite – aegirine syenite – urtite – ijolite association, such as Xiangshuigou and Aoyukou complexes; (3) clinopyroxenite – biotite clinopyroxenite – nelsonite – syenite association, representative complexes usually host economic iron and phosphorous ore deposits such as Yaojiazhuang (this study) and Fanshan complexes (e.g., Mu and Yan, 1992; Zhang, 1999; Jiang et al., 2004; Zhang et al., 2012; Hou et al., 2015).

Geology of Yaojiazhuang Ultrapotassic Complex

The *ca.* 221 Ma Yaojiazhuang ultrapotassic complex (Zhang et al., 2012) is an oval-shaped intrusive body in plan with a

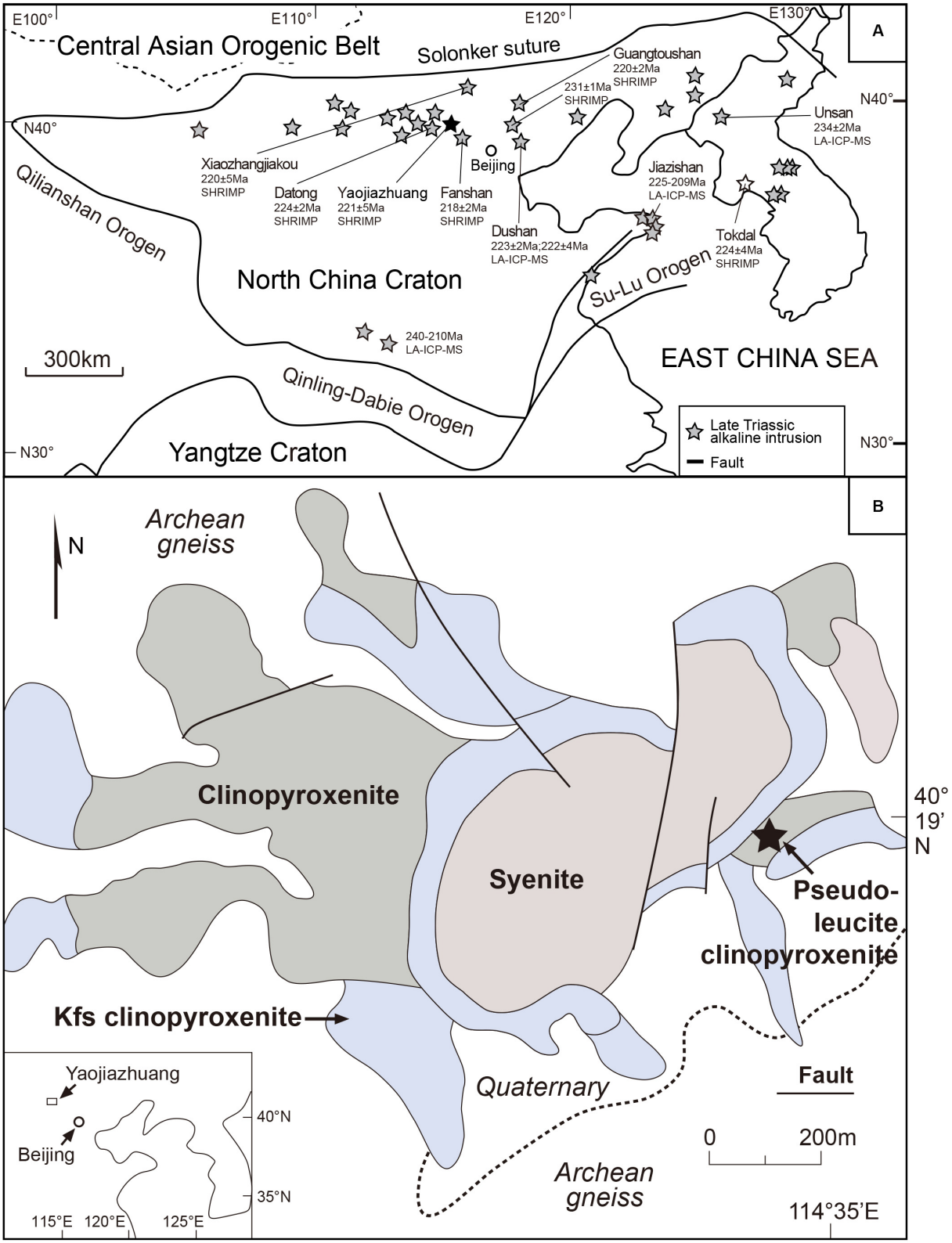

FIGURE 1 | (A) Simplified tectonic map showing the distribution of Late Triassic alkaline intrusions in North China Craton (modified from Ren et al., 2009). Labeled ages and analytical methods are compiled from Zhang et al. (2012) and references therein. **(B)** Geological map of Yaojiazhuang ultrapotassic complex modified from Hou (1990a).

size around 1.8 × 1.3 km (**Figure 1B**). It intruded the Archean gneiss and consists of a "bi-model" lithology with syenite at the core and clinopyroxenite at the periphery. At the places where they directly contacted, mingling between syenite and clinopyroxenite is observed (**Figure 2A**). In some parts of the complex, K-feldspar clinopyroxenite is outcropped either between the units of syenite and clinopyroxenite or scattered adjacent to the clinopyroxenite (**Figure 2B**). Besides, some clinopyroxenite host cm-sized pseudoleucite which had been previously identified as K-feldspar clinopyroxenite. At the upper part of clinopyroxenite, i.e., toward to syenite, the amount of apatite increased continuously, forming porphyritic or spheroidal apatite + magnetite ores up to around 10 cm (**Figure 2C**). These apatite clusters are cemented by a mineral assemblage resemble to clinopyroxenite. Coarsening of biotite is also observed locally, thus rocks in these places become extremely fragile (**Figure 2D**). Pegmatitic syenites occurred at the center of the syenite unit (**Figure 2E**) and aegirine syenite is locally present. Moreover, except the main units as mentioned above, late stage intrusive activities are quite vigorous, almost

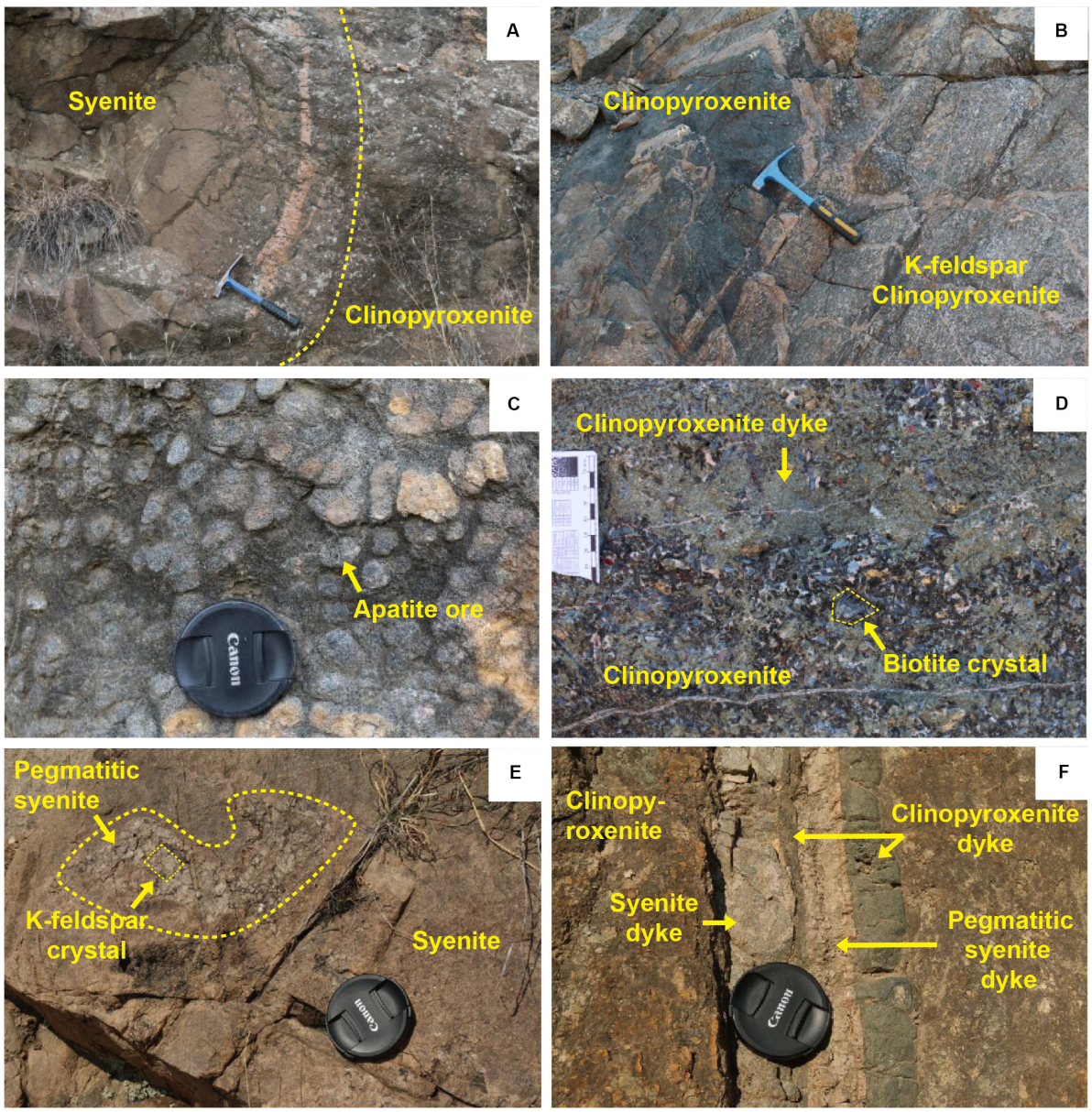

FIGURE 2 | Field photos showing the geology of Yaojiazhuang ultrapotassic intrusion. **(A)** Angular clinopyroxenite breccia at the boundary between syenite and clinopyroxenite. **(B)** Magma mingling between syenite and clinopyroxenite. **(C)** Intrusive contact between clinopyroxenite and K-feldspar clinopyroxenite. **(D)** Spheroidal apatite ores in clinopyroxenite. **(E)** Pegmatitic syenite at the center of the syenite unit. **(F)** Clinopyroxenite, syenite and pegmatitic syenite feeder dykes in the clinopyroxenite.

all the rocks in the Yaojiazhuang complex are cut by dykes with various compositions (**Figure 2F**).

ANALYTICAL METHOD

Scanning Electron Microscope

Polished thin sections were firstly mapped using a Zeiss Ultra 55 FESEM equipped with an INCA MAX 20 electron dispersive spectrometry (EDS) system at the Key Laboratory of Submarine Geosciences State Oceanic Administration, Second Institute of Oceanography, Ministry of Natural Resources (SIOMNR), China. The employed accelerating voltage was 15 kV.

Whole-Rock Major and Trace Elements

Samples were firstly peeled off the weathered or altered surfaces before jaw-crushing and the subsequent grounding in agate mills to powders of over 200 mesh. The pseudoleucite clinopyroxenites were initially packaged in a plastic envelope and crushed by hammering to small pieces, and then those pieces of as much as pure pseudoleucite or matrix were separately collected by hands and grounded to powders of ∼200 mesh in an agate mill. Major elements were analyzed by X-ray fluorescence (XRF) on fused glass discs at the laboratory of Nanjing Hongchuang Exploration Technology Service Co., Ltd. (NHETS) in Nanjing, China. The analytical uncertainties are < 1%, estimated from repeated analyses of 10 standards (GBW07101, GBW07103, GBW07105, GBW07114, AGV-2, BHVO-2, COQ-1, DTS-2b, GSP-2, and W-2a). Trace element data was determined by inductively-coupled–plasma mass-spectrometry (ICP-MS) after acid digestion of powders in high-pressure Teflon bullets performed at NHETS. The analytical precision for trace and rare earth elements is generally better than 10%, verified by repeated analyses of eight standards (GBW07103, GBW07316, BCR-2, W-2a, GSP-2, DTS-2b, BHVO-2, and AGV-2).

Electron Microprobe Analysis

Compositions of mineral phases were analyzed at SIOMNR using a JXA-8100 electron probe micro-analyzer (EPMA). Operating conditions were performed at 15 kV accelerating voltage with a 20 nA beam current. The beam size was 5 μm or 1 and up to 15 μm depending on crystal sizes. The peaks are counted by 10 s with background half of that for every element and ZAF method is employed in calibration. The standard reference samples are provided by National Technical Committee for Standardization of Microbeam Analysis (China) or produced by SPI Supplies® (America). The analytical precision was better than 5%.

PETROGRAPHY

Clinopyroxenite

Medium- to coarse-grained clinopyroxenite is commonly composed of > 60 mol.% of euhedral columnar (up to 2 mm in length) clinopyroxene, as well as various amounts of anhedral biotite and K-feldspar, and minor accessory minerals mainly including apatite, magnetite and analcite (**Figure 3**). The oriented euhedral cumulate clinopyroxene are commonly seen as imbedded crystal hosted in biotite, titanite and K-feldspar (**Figures 3A,B**) forming poikilitic texture. Besides, most of the cumulus clinopyroxene is compositionally zoned. Except occurring as oikocryst, K-feldspars also occur as fine-grained crystals coexisting with analcite in between clinopyroxene crystals (**Figure 3C**). Occasionally, biotite constitutes up to 50 mol.% of the rock and becomes euhedral with size up to 3 mm thus forming biotite clinopyroxenite and even glimmerite (**Figure 3D**). Euhedral apatite (0.1–0.5 mm in diameter), magnetite (0.1–1.0 mm) and occasionally ilmenite (∼0.1 mm) are presented as minor phases, and in some biotite rich area apatite can reach 15 mol.% to form apatite ores. Additionally, at some contact boundaries of minerals, magnetite is more well-formed than apatite but less than clinopyroxene (**Figure 3C**). Moreover, the presence of veins of pure analcite with width of 1–2 mm are ubiquitous in the clinopyroxenite (**Figure 3E**). These veins are commonly composed of (1) analcite; (2) K-feldspar with exsolved lamellae of albite, which are approximately right to the vein); and (3) biotite, occasionally hosting anhedral clinopyroxene inclusions. The clinopyroxene adjacent to these veins is euhedral and usually rimmed by a darker greenish corona of clinopyroxene.

K-Feldspar Clinopyroxenite

K-feldspar clinopyroxenite is transitional in term of mineral assemblage and crystal mode between syenite and clinopyroxenite. These rocks are dark reddish in color and relatively coarse-grained in hand specimen scale, and mainly consists of euhedral K-feldspar and clinopyroxene, with anhedral biotite. The modal proportion of the three main minerals vary from place to place. The euhedral tabular K-feldspar usually vary from 1 to 7–8 cm in length and are preferentially orientated. The occurrence of clinopyroxene and biotite are constrained in the interstices between K-feldspar crystals. They usually exhibit poikilitic texture similar to the clinopyroxenites, whereas minor titanite (1–2 mm) occurs as individual grain (**Figure 3F**). Minor apatite (<1 mm) also exists as interstitial phase. In addition, some veins with 1–2 mm width are filled by analcite are commonly present in the K-feldspar clinopyroxenite as well.

Pseudoleucite Clinopyroxenite

Pseudoleucite clinopyroxenite is characterized by leucocratic pseudoleucite or cluster of pseudoleucite embedded in the melanocratic matrix (**Figure 4A**), which are predominantly composed of biotite, clinopyroxene, and subordinate garnet, apatite, magnetite and K-feldspar. Most of the pseudoleucite crystals are generally euhedral to subhedral, with the typical shape of leucite with ∼1 cm in diameter (**Figure 4B**).

Similar to some of the pseudoleucite reported (Gittins et al., 1980; Comin-Chiaramonti et al., 2009), the pseudoleucite in Yaojiazhuang consists of dominantly fine-grained K-feldspar (∼50 mol.%, 5–40 μm), nepheline (∼30 mol.%, 5–20 μm) and muscovite (∼15 mol.%, 5–20 μm) intergrowth at the core and nearly pure fine-grained K-feldspar at the rim (**Figure 4**). The fringes of the intergrowth are vermicular or flame-like or

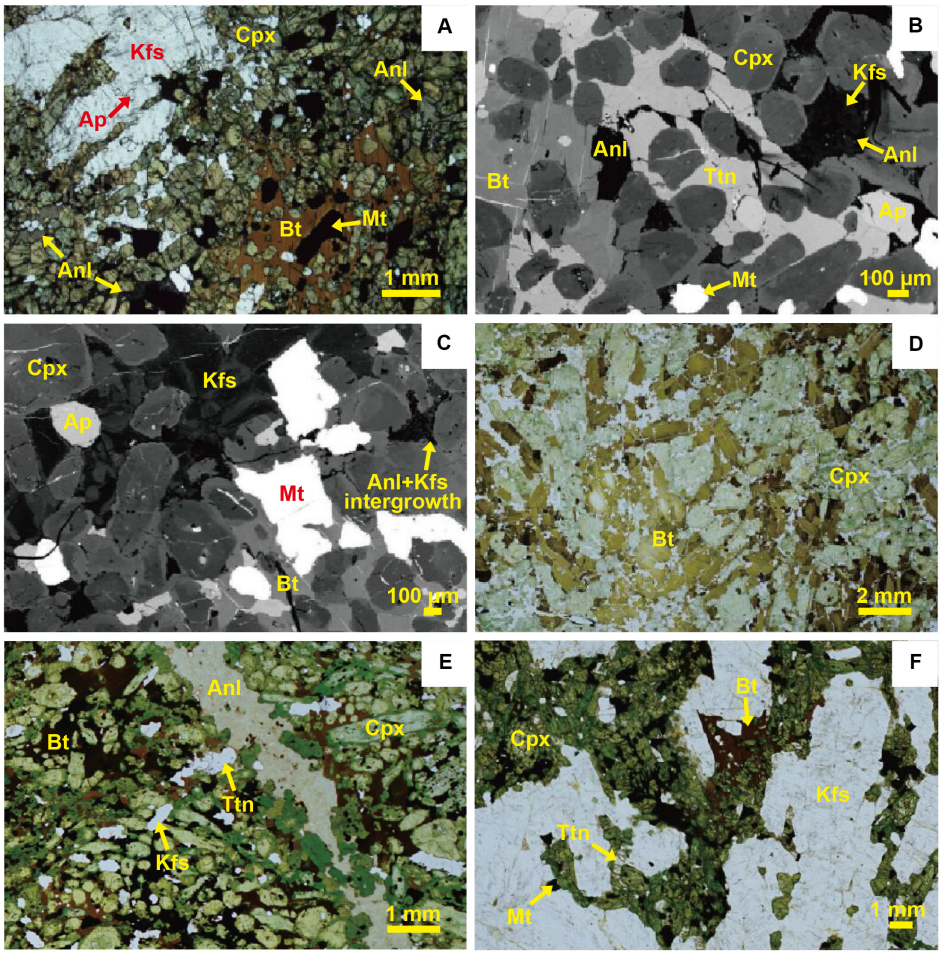

FIGURE 3 | Microphotos of clinopyroxenite. **(A)** Poikilitic texture with zoned clinopyroxene chadacrysts and biotite and K-feldspar oikocrysts (plane-polarized light). **(B)** Titanite oikocrysts (Back-scattered electron, BSE, image); There are also micro co-existing K-feldspar and analcite at the upright part of the picture. **(C)** Zonation of K-feldspar oikocryst, and there are micro co-existing K-feldspar and analcite at the upright part of the picture (BSE image). **(D)** Glimmerite (scanned photo of thin section). **(E)** A vein filled by analcite (scanned photo of thin section). **(F)** K-felspar clinopyroxenite showing poikilitic texture in the interstices between K-feldspar grains (scanned photo of thin section). Ap, apatite; Anl, analcite; Bt, biotite; Cpx, Clinopyroxene; Kfs, K-feldspar; Mt, Magnetite; Ttn, titanite.

feather-like and usually perpendicular to the boundaries of the pseudoleucite grains. Within some pseudoleucite, coarsening of euhedral prismatic to granular nephelines up to ∼200 μm is observed coexisting with K-feldspar, whereas many of these nephelines have been altered to kaolin and corundum (**Figure 4F**). Some anhedral (sub-round to round) and zoned K-feldspars (hundreds of μm) occasionally exhibit lineation and present either across or at the edge of the pseudoleucites (**Figures 4E,F**). Adjacent to the K-feldspar lineation, shapeless intergrowth of nepheline with muscovite or plus analcite pools and patches usually occur. Within some pseudoleucite crystals, nephelines are totally replaced by analcites, even in the vermicular intergrowths, and in such places, the amount of muscovite also increased accordingly. Individual mineral inclusions are prevalent in the pseudoleucite, predominantly laminar biotite (5 mol.%; tens of μm) and accessory celestine (∼10 μm), titanite (up to ∼100 μm), apatite (tens of 10 μm), calcite (up to 100 μm; **Figure 5A**) and magnetite (∼10 μm). Minor zoned clinopyroxene inclusions (several to > 100 of μm) only occur as clusters and are rather rare (**Figure 5B**).

The matrix comprises mainly euhedral biotite (0.1–1 mm), clinopyroxene (0.1–1.5 mm) and garnet (0.01–1 mm). These phases contribute ∼85 mol.% of the total amount of matrix but the individual proportions for different phases vary from place to place. In most cases, columnar clinopyroxene and laminar biotite are showing a preferred orientation consistent with the boundary line of the globules. Clinopyroxene commonly shows complex zonation (**Figure 5C**), for example, a core of relics or clastic of clinopyroxene with visible zonation, rimmed also by zoned clinopyroxene (**Figure 5D**). Euhedral apatite (20–200 μm), subhedral to anhedral magnetite (<50 μm) and anhedral K-feldspar (10–300 μm) account for 15 mol.% of the matrix. Apatite crystals are usually enclosed by garnets (**Figure 5E**). Other minor phases include analcite (<30 μm), titanite (20–200 μm), muscovite (several micrometers), calcite (several

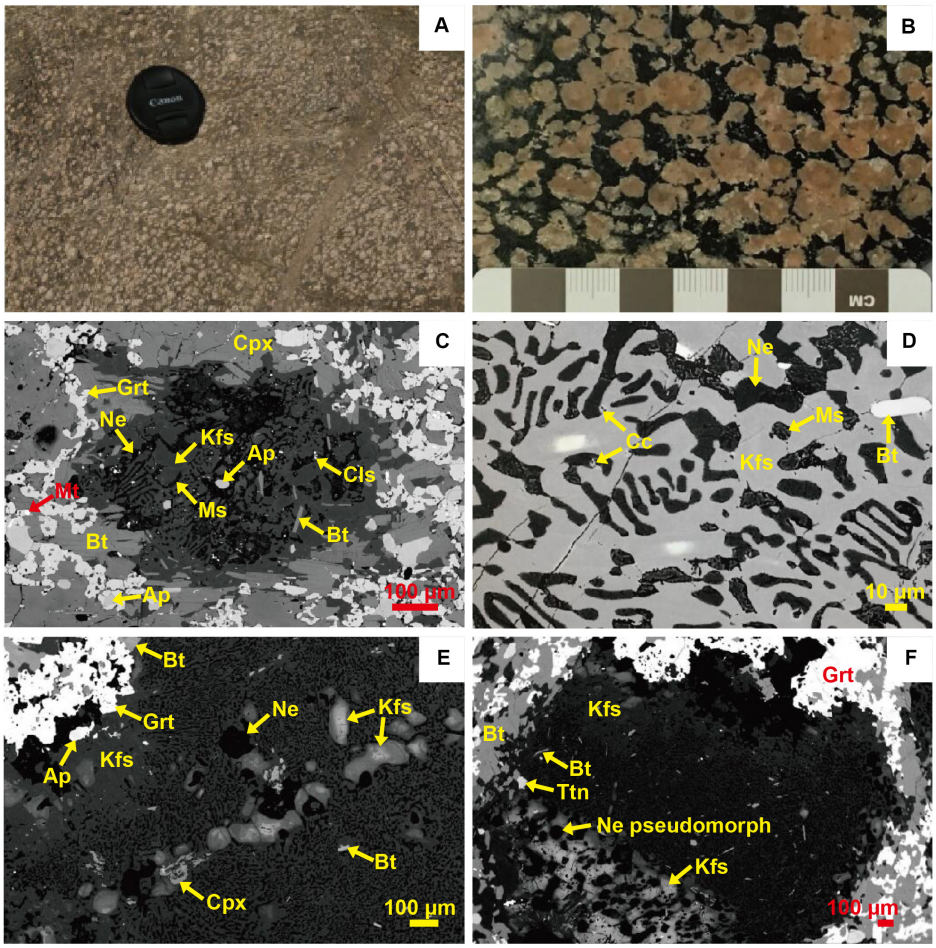

FIGURE 4 | Photos of pseudoleucite clinopyroxenite. **(A)** Field photo. **(B)** A polished hand specimen. **(C)** A representative pseudoleucite and the mineral phases in both of the pseudoleucite and the matrix (BSE image). **(D)** Vermicular intergrowth of K-feldspar, nepheline and muscovite (BSE image). **(E)** Compositionally zoned K-feldspars clusters in a lineation (BSE image). **(F)** Coarse nepheline pseudomorphs in the compositionally zoned K-feldspars (BSE image). Cc, Calcite; Cls, Celestine; Grt, garnet; Ms, Muscovite; Ne, Nepheline; others are as before.

micrometers) and ilvaite (∼10 μm). Micro intergrowth of nepheline or analcite with K-feldspar is also observed as shapeless interstitial phases. Euhedral granular analcites are found in clinopyroxenes with expansion cracks in the host minerals (**Figure 5F**).

Syenite

The syenite is pale red in color and consists of mainly oriented euhedral to subhedral K-feldspar (>70 mol.%, 0.1–3 mm), clinopyroxene (10–15 mol.%, 0.1–2 mm). Pegmatitic syenite is observed at the center of syenite (**Figure 2E**), where the length of K-feldspar can be up to 10 mm. The K-feldspar crystals commonly host exsolved albite lamellae, and in those samples collected at the center of the syenite, zonation of K-feldspar is observed (**Figure 6A**). Anhedral clinopyroxene grains commonly show compositional zonation, and in some samples near the clinopyroxenite, they are in round shape with a diameter about 100 μm scattering among the K-feldspars (**Figure 6B**). In the syenite near the clinopyroxenite, small (<50 μm) acicular-shaped clinopyroxene crystals are observed in the hosted K-feldspar crystals (**Figure 6C**). Accessory phases include anhedral biotite (0.1–0.3 mm), analcite (tens of μm), apatite (∼100 μm), titanite (tens of μm), magnetite (several to tens of μm) and calcite (∼10 μm). The calcite usually co-exists with analcite and exsolved albite (**Figure 6D**). Anhedral amphibole surrounding clinopyroxene is occasionally observed in the samples from the center of the syenite (**Figure 6E**). Besides, analcite veins are usually observed in the syenite (**Figure 6F**). K-feldspar adjacent to the vein is euhedral and usually grows across the veins. Analcite lamellae is usually observed in these K-feldspar crystals.

Dykes

Mafic and syenitic dykes pervasively cut all the three major lithologic units in Yaojiazhuang complex. In the field, mafic dykes (commonly ∼10 cm wide) are greenish to dark gray in color. The mafic dykes are fine-grained, lithologically similar to the clinopyroxenite, consisting of mainly oriented euhedral clinopyroxene (<1 mm), biotite (<1 mm) and K-feldspar

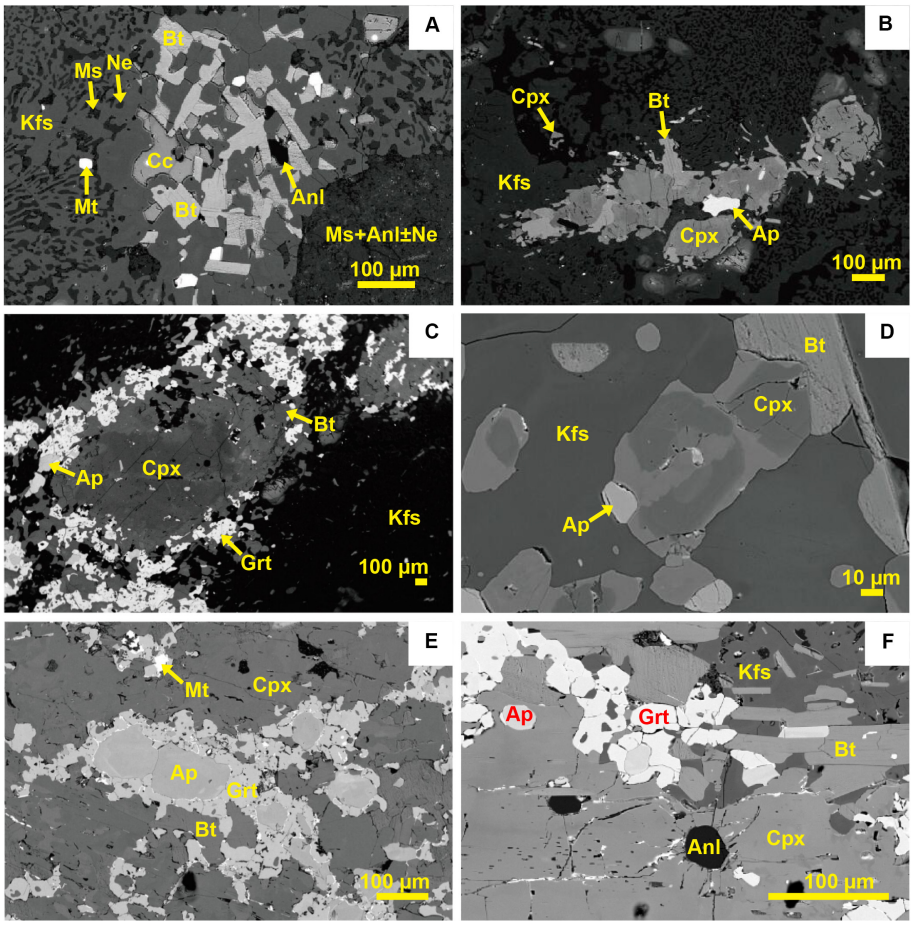

FIGURE 5 | Photos of pseudoleucite clinopyroxenite. **(A)** Calcite inclusion (BSE image). **(B)** Anhedral zoned clinopyroxene clusters as inclusions in pseudoleucite (BSE image). **(C)** Complex zonation of clinopyroxene in the matrix (BSE image). **(D)** A core of relics or clastic of clinopyroxene with visible zonation, rimmed also by zoned clinopyroxene (BSE image). **(E)** Apatite enclosed in garnets (BSE image). **(F)** Euhedral analcites in clinopyroxenes with expansion cracks (BSE image). Abbreviations are as before.

(<1 mm) of almost equal quantities (~30 mol.%). Analcite is commonly present in the interstices to form networks (~1 mm in width) separating the samples into different lithological parts (**Figure 7A**). In these analcite-rich zones, more clinopyroxene and biotite is observed. Minor phases include apatite, magnetite, and titanite are present.

According to the spatial relationship, both early and late stage syenitic dykes (commonly around 10 cm wide) had been recognized (**Figure 7B**). Nevertheless, the two stage dykes are similar in mineral assemblage and defined as clinopyroxene syenite. K-feldspar is the main phase in both of these two kinds of dykes (>80 mol.%) and hosts exsolved albite thin lamellae. Subordinary minerals are composed of biotite and clinopyroxene. Anhedral biotite mainly occurs as interstitial phases between K-feldspar grains. Small needle-like clinopyroxene is widespread in the host K-feldspar and biotite, which is interpreted as a result of quenching. Accessory minerals includes titanite, analcite and apatite. In some samples, euhedral titanite can grow up to 1–2 mm (**Figure 7C**). The late stage dyke is composed of K-feldspar, clinopyroxene, biotite with considerable amount of albite. K-feldspar accounts for 70% modal and its size is generally around 1–2 mm in length except some crystals could be up to 2–3 cm (**Figure 7D**). Clinopyroxene (20 mol.%) can be divided into at least two generations, one is as euhedral to subhedral zoned phenocryst up to 0.6 mm (**Figure 7E**), the other is as needle-shaped inclusions in the matrix commonly less than 50 μm in length. Clinopyroxene pseudomorph filled by albite, muscovite and magnetite is also observed (**Figure 7F**). Subhedral to anhedral biotite (<2 mm) constitutes the rest 10% modal percent. Anhedral albite is observed co-existing with K-feldspar either as exsolved lamellae or in the interstices of clinopyroxene and biotite crystals (**Figure 7E**). Euhedral titanite and apatite are also present as minor phases.

RESULTS

Scanning Electron Microprobe

Elements mapping (**Figure 8**) shows that the pseudoleucites are mainly enriched in Si, Al, Na, and K but poorer in Fe and Ca

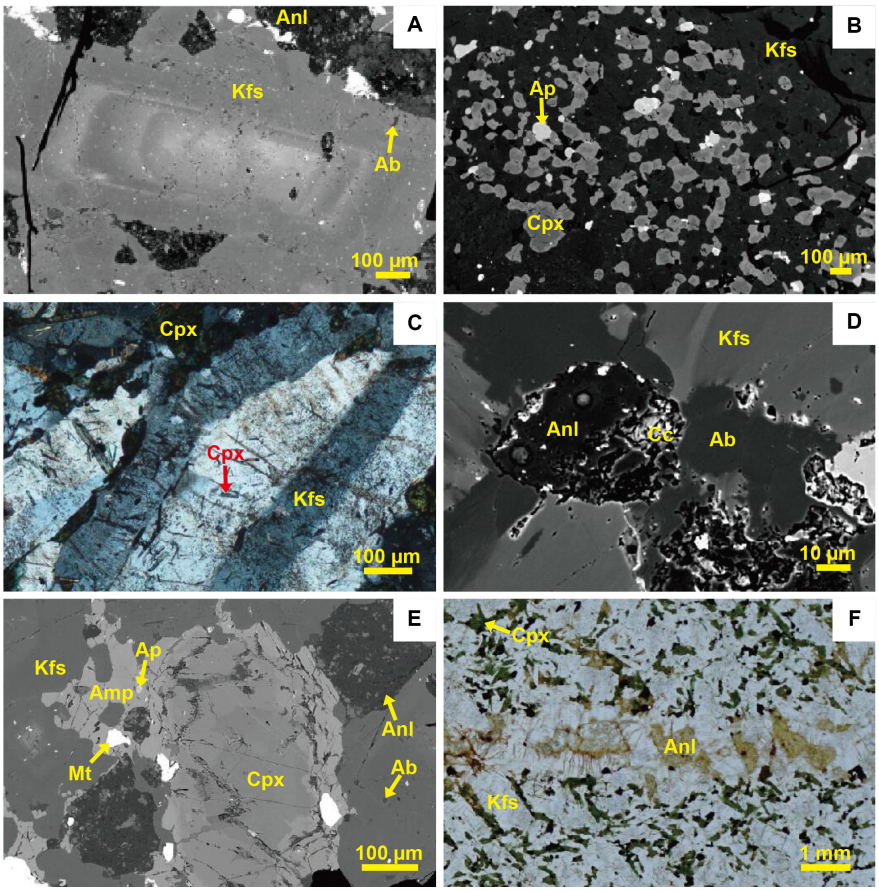

FIGURE 6 | Photos of syenite. **(A)** Zonation of K-feldspar in samples collected at the center of the syenite (BSE image). **(B)** Zoned anhedral clinopyroxenes scattered among K-feldspars (BSE image). **(C)** Acicular-shaped clinopyroxene crystals in the hosted K-feldspar crystals in the syenite samples close to the clinopyroxenite (plane-polarized light). **(D)** Co-existing K-feldspar, exsolved albite, analcite and calcite (BSE image). **(E)** Anhedral amphibole surrounds zoned clinopyroxene (BSE image). **(F)** Analcite vein (scanned photo of thin section). Ab, Albite; Amp, Amphibole; other abbreviations are as before.

relative to the matrix, which should be caused by the appearance of different minerals. The concentrations of elements within the pseudoleucites from edges to cores are relatively homogeneous, except that the compositionally zonation of K-feldspars slightly lack in Si and K. The coarse nepheline pseudomorphs are more enriched in Ca, Na but deficient in Fe compared to other parts of the pseudoleucite.

Whole-Rock Geochemistry

The whole-rock major and trace element analyses of the studied syenite, clinopyroxenite, pseudoleucite clinopyroxenite, as well as syenitic and clinopyroxenitic dykes from Yaojiazhuang alkaline complex are given in **Supplementary Table 1**.

Syenites generally display higher SiO_2 (57.2–64.1 wt.%), Al_2O_3 (16.6–18.8 wt.%), Na_2O (1.3–4.9 wt.%) and K_2O (8.0–11.1 wt.%) contents but lower CaO (1.0–2.2 wt.%), MgO (0.1–0.7 wt.%), total Fe_2O_3 (1.9–5.5 wt.%), and P_2O_5 (0.03–0.2 wt.%). Their molar K_2O/Na_2O ratios vary largely, from 1 to 5.7. The chemical composition of the syenitic dykes resemble that of syenites, containing 58.9–61.2 wt.% SiO_2, 15.5–18.6 wt.% Al_2O_3, 1.0–5.4 wt.% Na_2O, 7.1–12.8 wt.% K_2O, and relatively lower CaO (0.3–2.5 wt.%), MgO (0.3–1.1 wt.%), total Fe_2O_3 (1.5–6.4 wt.%) and neglectable P_2O_5 (0.03–0.2 wt.%), and also a wide molar K_2O/Na_2O variation (0.9–8.2). The late-stage syenitic dyke (YJZ04-3) contains the highest Na_2O content (5.4 wt.%) among all syenitic rocks but the lowest K_2O content (7.1 wt.%) and molar K_2O/Na_2O ratio (0.8).

In general, clinopyroxenites and biotite clinopyroxenites are characterized by relatively higher CaO (15.2–18.15), MgO (9.6–12 wt.%), total Fe_2O_3 (11.4–21.2 wt.%), TiO_2 (1.6–1.7 wt.%) and P_2O_5 (1.9–3.4 wt.%) but lower SiO_2 (40.9–42.7 wt.%), Al_2O_3 (4–7 wt.%), Na_2O (0.5–0.9 wt.%), and molar K_2O/Na_2O (1.1–4.8). Differently, K-feldspar clinopyroxenite show relatively lower CaO (4–7.5 wt.%), MgO (1.4–4.8 wt.%), total Fe_2O_3 (6–9.4 wt.%), TiO_2 (0.6–1.4 wt.%), and P_2O_5 (0.3–1.3 wt.%) but higher SiO_2 (50.6–57 wt.%), Al_2O_3 (12.1–16.3 wt.%), Na_2O (1–3.5 wt.%), and molar K_2O/Na_2O (1.4–5.5) compared to (biotite) clinopyroxenites. The clinopyroxenite dyke exhibit an moderate composition between (biotite) clinopyroxenite and K-feldspar clinopyroxenite (49 wt.% SiO_2, 11.6 wt.% total Fe_2O_3, 6.8 wt.% MgO, 7.8 wt.% CaO, 11.6 wt.% Al_2O_3, and 2 wt.% P_2O_5), indicating the cumulations of mafic minerals such as

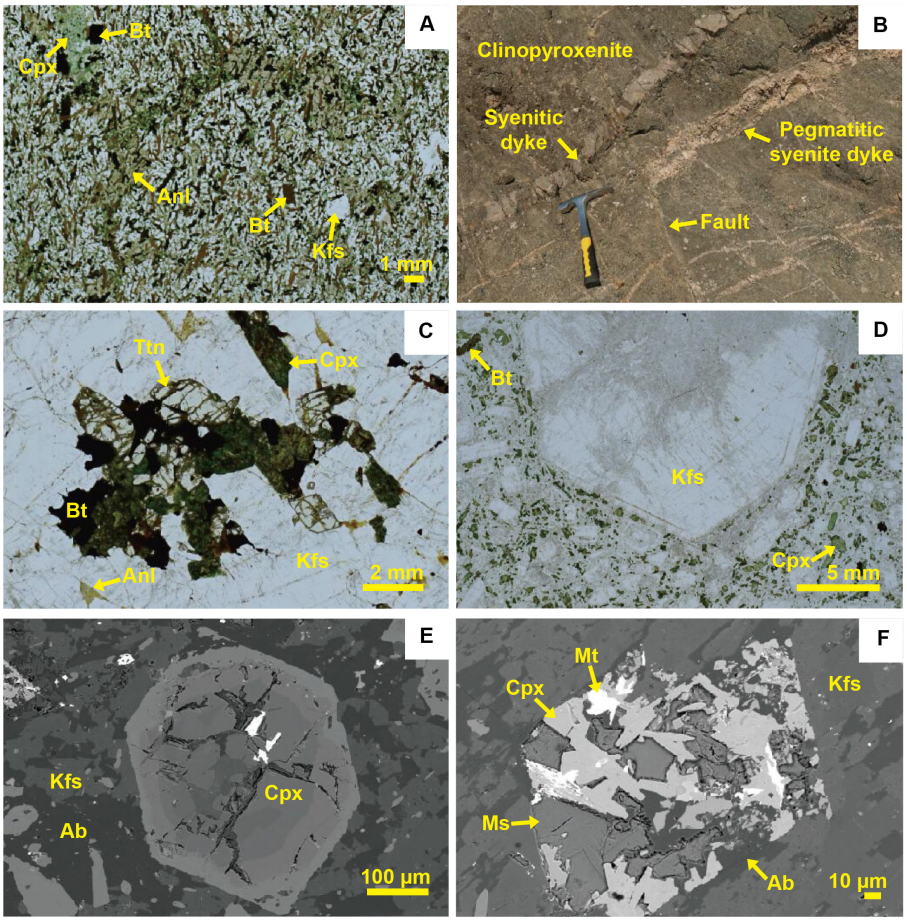

FIGURE 7 | Petrographic photos of dykes. **(A)** Clinopyroxenite dyke showing the analcite network (scanned photo of thin section). **(B)** Field photo showing the relationship between syenitic dykes and faults. **(C)** Coarse euhedral titanite in late-stage syenitic dyke (scanned photo of thin section). **(D)** Pegmatitic K-feldspar crystal in late-stage syenitic dyke (scanned photo of thin-section). **(E)** Euhedral zoned clinopyroxene with aegirine rim, also showing the albite exsolution in the matrix (BSE image). **(F)** Clinopyroxene replaced by muscovite, magnetite and albite (BSE image). Abbreviations are as before.

clinopyroxenite, apatite and magnetite in the formation of (biotite) clinopyroxenites, and progressively high proportions of felsic minerals like K-feldspar in K-feldspar clinopyroxenites. On the Harker diagram (**Figure 9**), the composition of (biotite) clinopyroxneites, K-feldspar clinopyroxenites, syenites and dykes exhibit significant linear correlations among many elements such as FeO_T, MgO and CaO, implying that the geochemical evolution of Yaojiazhuang samples from clinopyroxnites to syenites are mainly controlled by successive accumulation and subtraction of cumulate minerals.

The composition of pseudoleucite clinopyroxenite matrix resembles those of clinopyroxenites and is characterized by relatively high total Fe_2O_3 (21.1 wt.%) and CaO (15.9 wt.%), moderate MgO (7.1 wt.%), Al_2O_3 (7.3 wt.%), K_2O (4.4 wt.%), and P_2O_5 (1.6 wt.%) but low SiO_2 (38.9 wt.%) and Na_2O (0.5 wt.%). On the contrast, the pseudoleucite contains higher SiO_2 (57.0 wt.%), Al_2O_3 (23.8 wt.%), Na_2O (2.2 wt.%), and K_2O (11.5 wt.%) but lower CaO (0.8 wt.%), MgO (0.4 wt.%), total Fe_2O_3 (0.8 wt.%), and negligible P_2O_5. Both of the psudoleucite and matrix have high molar K_2O/Na_2O ratios, which are 3.4 and 5.6 respectively. The pseudoleucite also displays a high LOI value (3.9 wt.%), which is dominantly contributed by the contents of H_2O^+ (3 wt.%) and CO_2 (0.4 wt.%).

The trace element and rare earth element (REE) compositions of the Yaojiazhuang intrusion are given in **Supplementary Table 1** and illustrated in chondrite-normalized and primitive mantle-normalized diagrams in **Figure 10**. In general, (biotite) clinopyroxenites have higher REE contents than syenites, and the matrix of pseudoleucite clinopyroxenite has the highest. K-feldspar clinopyroxenites contain moderate REE contents between (biotite) clinopyroxenites and syenites. For most REEs and trace elements, the contents in pseudoleucite are very low, which may be inherited from the extremely low partition coefficients in leucite. All the rock types are characterized by significant enrichment in highly incompatible elements and light REE. Notably on the spider diagram, (biotite) clinopyroxenites and K-feldspar clinopyroxenites show a variation of P from positive anomaly to negative anomaly, symmetrical about that of the clinopyroxenite dyke, implying the fractionation/cumulation of apatite to form apatite ore hosted in clinopyroxenites.

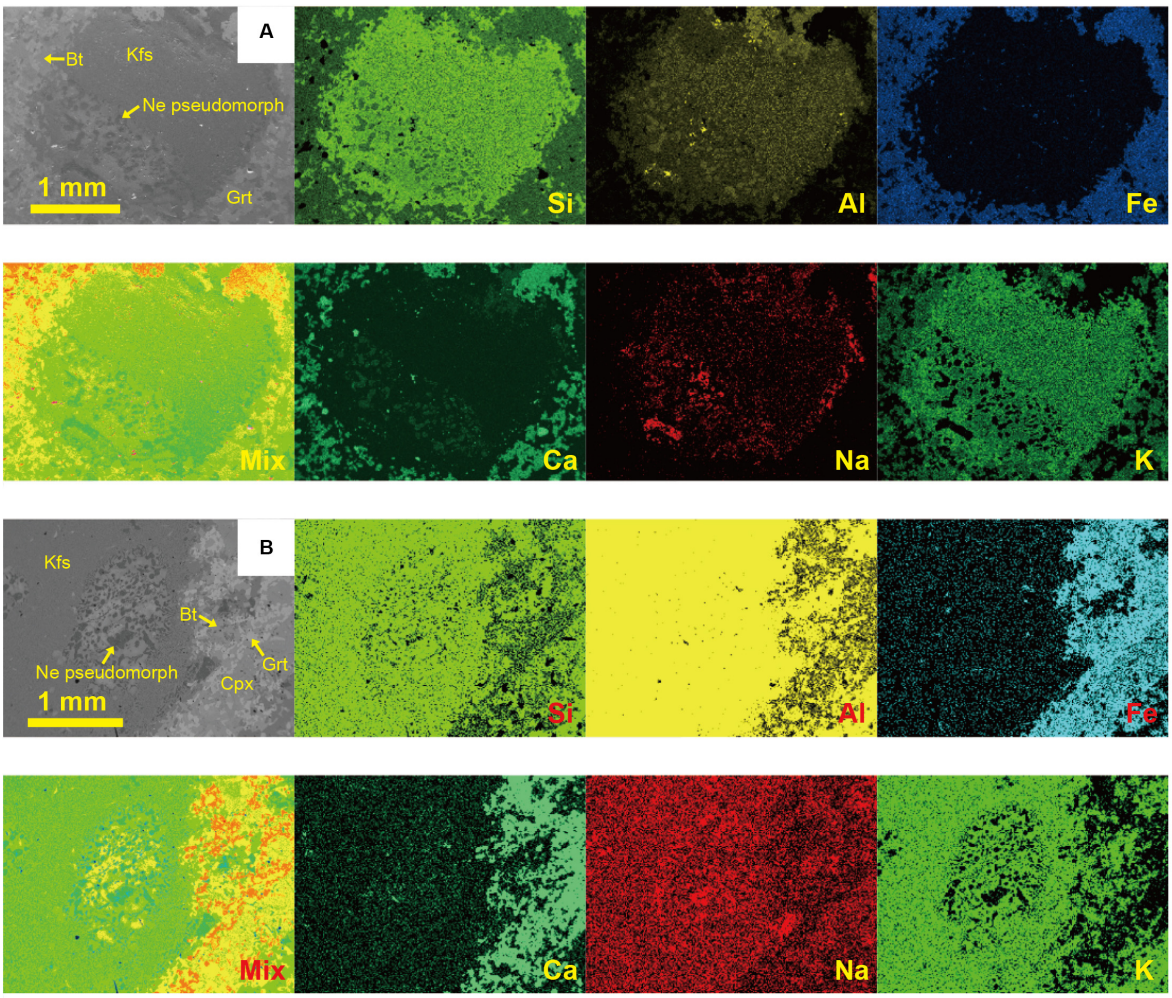

FIGURE 8 | Secondary electrons and scanning electron microscope (SEM) images of the pseudoleucite clinopyroxenite. **(A)** A pseudoleucite (**Figure 4F**) surrounded by the matrix. **(B)** The boundary between pseudoleucite and matrix.

The (biotite) clinopyroxenite and the matrix of pseudoleucite clinopyroxenite exhibit a distinct enrichment in high field-strength element compared to syenite and pseudoleucite. The pseudoleucite is significantly enriched in large ion lithophile elements (LILE), such as K, Rb, Ba, and Sr, commonly higher than those of syenites. In the REE patterns, all of rock types have similar slopes, whilst the concentrations of REE in clinopyroxenites and the pseudoleucite clinopyroxenite matrix are much higher than other samples. Despite two syenitic dykes, other samples do not show distinct Eu anomaly, with $(Eu/Eu^*)_N$ values generally vary around 1.

Mineral Chemistry

Silicates

Silicate minerals in Yaojiazhuang complex include clinopyroxene, K-feldspar, biotite, muscovite, garnet, nepheline, analcite, amphibole, apatite and titanite, and their compositions by EMPA are given in **Supplementary Table 2**.

Clinopyroxenes in all lithologies of the Yaojiazhuang intrusion generally show zonings with a Mg-rich core and an Fe-rich rim (**Figure 11A**). Zoned clinopyroxene has a composition of $Wo_{44.1-47.4}En_{34.7-42.8}Fs_{9.3-15.7}Ac_{1.0-4.2}$ in the core and to $Wo_{35.3-44.8}En_{20.5-29.5}Fs_{20.5-28.8}Ac_{5.2-15.3}$ in the rim (**Figure 11A**). Rims are usually become rich in Na, indicated by the high Ac endmember. Interestingly, the clinopyroxenes in both of pseudoleucite and the matrix of pseudoleucite clinopyroxenite are similar in composition as well. A compositional profile of a clinopyroxene crystal with oscillatory zonings in clinopyroxenite is shown in **Figure 12A**. Aegirine is widely recognized in the late-stage clinopyroxene syenite dykes with a composition of $Wo_{11.1}En_{6.3}Fs_{40.5}Ac_{40.2}$. A profile of a zoned clinopyroxene in this syenite dyke is shown in **Figure 12C** with an augite core and aegirine rim.

K-feldspars in the syenites in the center of the complex and the late-stage syenite dykes exhibit a relatively large compositional rang of $Or_{52.6-74.8}Ab_{24.9-46.5}An_{0.3-1.0}$. In contrast, K-feldspars in other parts of the Yaojiazhuang complex

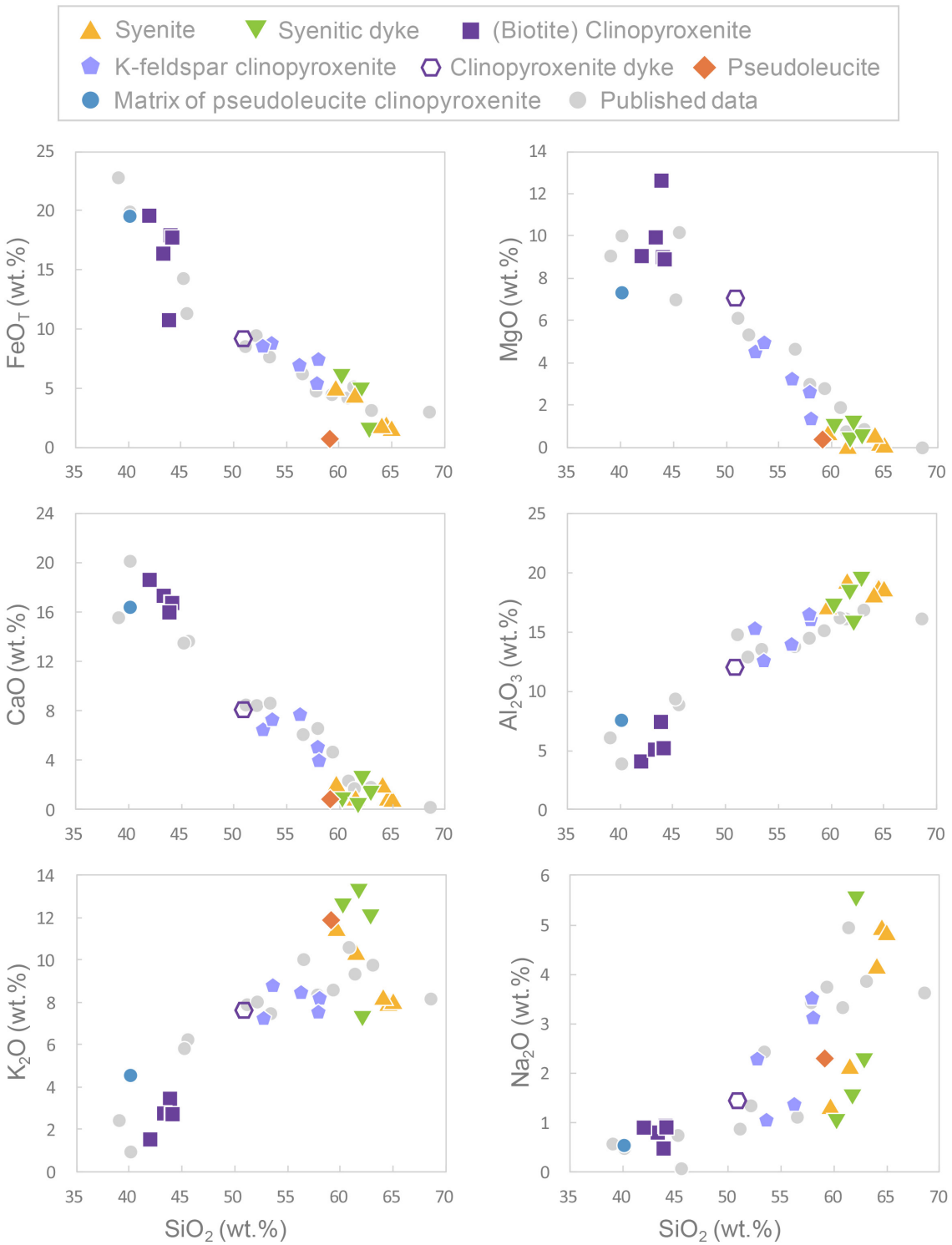

FIGURE 9 | Harker diagrams of the syenite, (biotite) clinopyroxenite, K-feldspar clinopyroxenite, pseudoleucite and matrix of the pseudoleucite clinopyroxenite rocks, and dykes. Published data of Yaojiazhuang complex are from Mu and Yan (1992) and Chen et al. (2013).

are almost pure orthoclase, showing restricted compositional variation of $Or_{86.2-95.0}Ab_{4.8-13.8}An_{0.0-0.3}$ (**Figure 11B**). For example, the compositions of K-feldspar in both of psudoleucite and matrix of pseudoleucite clinopyroxenite are almost pure orthoclase. Notably, albite is observed coexisting with K-feldspar as exsolved lamellae in clinopyroxenite, syenite and syenitic dykes

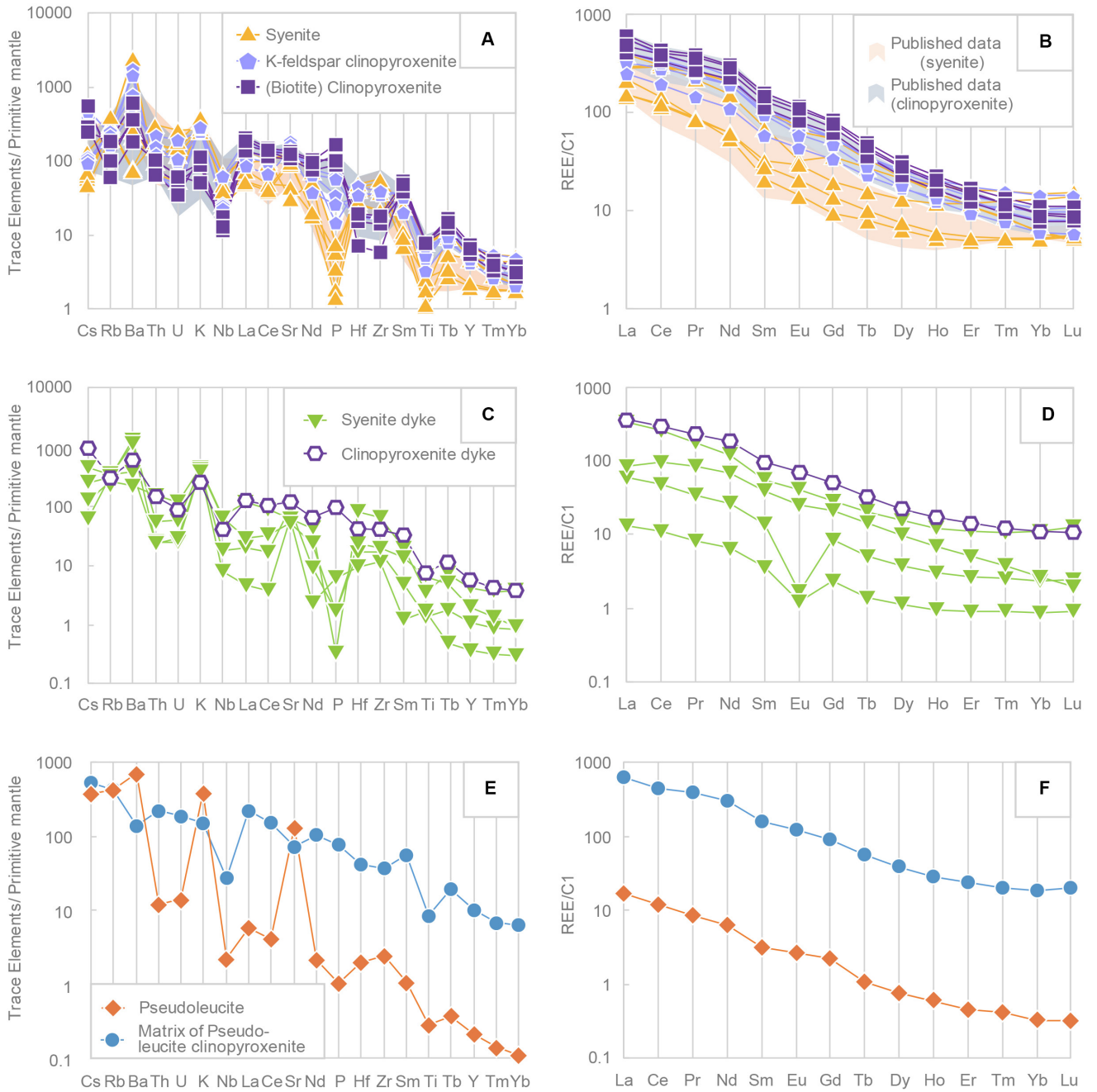

FIGURE 10 | Primitive mantle normalized trace element spider diagram of **(A)** syenite, (biotite) clinopyroxenite and K-feldspar clinopyroxenite; **(C)** syenitic and clinopyroxenitic dykes; **(E)** pseudoleucite and matrix of the pseudoleucite clinopyroxenite; chondrite normalized rare earth element (REE) pattern of **(B)** syenite, (biotite) clinopyroxenite and K-feldspar clinopyroxenite; **(D)** syenitic and clinopyroxene dykes; **(F)** pseudoleucite and matrix of the pseudoleucite clinopyroxenite. Published data of Yaojiazhuang complex are from Mu and Yan (1992) and Chen et al. (2013). The primitive mantle and C1 chondrite normalizing values are from Sun and McDonough (1989).

with composition $Or_{0.4-1.6}Ab_{91.6-99.3}An_{0.3-7.2}$. The most An-rich feldspar (An = ~7) is found in the syenites in the center of the complex, where that zonation of K-feldspar with an Or-rich core and an Ab-rich rim is commonly observed (**Figure 12B**).

The composition of biotite in the Yaojiazhuang complex show restricted range, with FeO_{tot} from 18.2 to 23.6 wt.%, MgO from 10.4 to 14.2 wt.%, TiO_2 from 1.8 to 2.5 wt.%, and K_2O from 9.4 to 9.8 wt.%. Accordingly, the biotite can be classified into the siderophylite group on the Fe/(Fe + Mg)–ΣAl diagram (**Figure 11C**).

All the analyses of garnets are Fe- (24.9–25.4 wt.%) and Ti-rich (1.6–4.8 wt.%) and occupy a limited compositional range

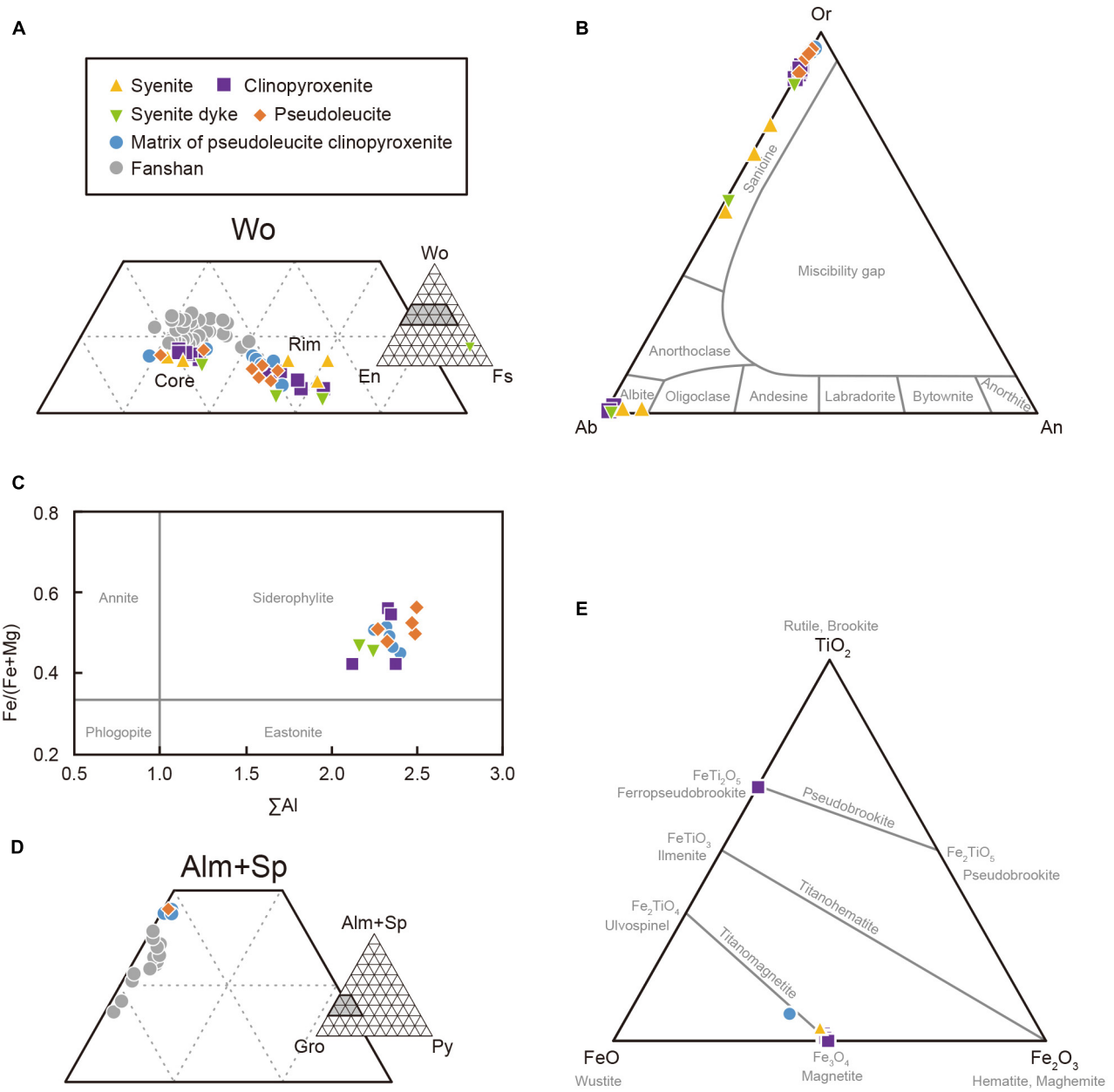

FIGURE 11 | Compositional variation of major minerals from Yaojiazhuang complex. **(A)** Clinopyroxene; **(B)** K-feldspar with exsolved albite lamellae; **(C)** biotite; **(D)** garnet; **(E)** TiO_2–FeO–Fe_2O_3 ternary system (after Buddington and Lindsley, 1964). Data of clinopyroxenes and garnets from Fanshan ultrapotassic complex (Hou et al., 2015) are plotted for comparison.

on the Alm + Sp–Gro–Py diagram (Coleman et al., 1965; **Figure 11D**), which are essentially grossular (61.2–61.7%) and almandine (37.3–37.6%). However, compared to those from Fanshan complex unit 3 clinopyroxenite, whose FeO content commonly below 22 wt.% and TiO_2 above 5 wt.% (up to 12.3 wt.%), these garnets are richer in FeO but poorer in TiO_2.

Amphiboles found in both of clinopyroxenite and syenite are classified as ferro-pargasite, which is characterized by the significant high content of FeO_{tot} (20.1–20.1 wt.%). The contents of SiO_2, TiO_2, MgO, CaO, Na_2O, and K_2O are 39.6–40.1 wt.%, 1.1–1.5 wt.%, 8.5–9.5 wt.%, 10.4–10.5 wt.%, 2.8–3.2 wt.%, and 1.9–2.0 wt.%, respectively. Notably, the amphiboles in our samples also contain 0.8–0.9 wt.% F.

Apatites are nearly pure fluorapatite characterized by X_F [= molecular F/(F + Cl)] very close to 1.00 with high F (2.1–3.4 wt.%) relative to low Cl contents (<0.02 wt.%), which implies that they may crystallized from a high temperature, i.e., magmatic environment (Tacker and Stormer, 1989). Other oxides contents in all three lithology units exhibit no obvious differences, with

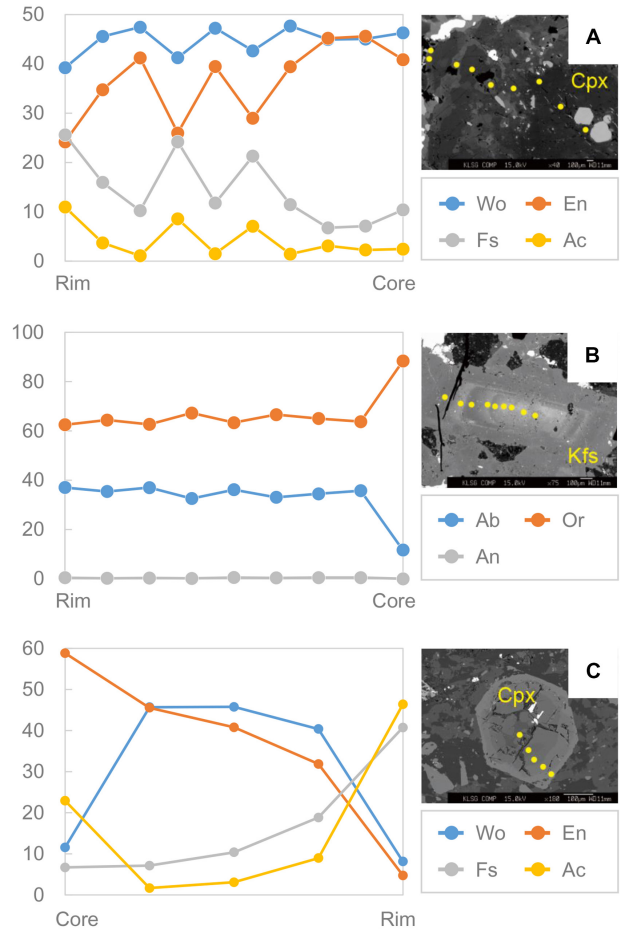

FIGURE 12 | Compositional profiles of zoned minerals. **(A)** A giant clinopyroxene crystal in the clinopyroxenite; **(B)** K-feldspar in the samples collected from the center of syenite; **(C)** A clinopyroxene (**Figure 7E**) in the late-stage syenite dyke.

SiO_2, CaO, and P_2O_5 contents are 0.4–1.0 wt.%, 50.6–53.1 wt.%, and 38.5–41.4 wt.% respectively.

The composition of nepheline is relatively identical in all pseudoleucite samples, the SiO_2, Al_2O_3, Na_2O, and K_2O contents of which are 41.5–42.6 wt.%, 34.2–34.5 wt.%, 15.8–16.1 wt.%, and 5.9–7.5 wt.%, respectively, while its CaO content is extremely low, which is 0.1–0.6 wt.%. Analcites are characterized by containing high sodium and water contents, with Na_2O contents are 11.3–12.5 wt.%, and total values range from 89.4 to 92.4 wt.%. The SiO_2 (52.2–56.3 wt.%), Al_2O_3 (22.8–25.7 wt.%) and K_2O (0.2–0.5 wt.%) contents vary limitedly.

Muscovites from all of the lithologies do not show significant difference, and show SiO_2 contents from 43.8 to 45.3 wt.%, Al_2O_3 from 34.9 to 38.2 wt.%, K_2O from 9.0 to 11.2 wt.%, FeO from 0.4 to 3.9 wt.%, MgO up to 1.6 wt.% and total values generally between 93 and 96 wt.%. The SiO_2, TiO_2 and CaO contents of titanite are 28.9–30.0 wt.%, 34.4–38.0 wt.%, and 25.8–27.4 wt.%, respectively, together with 0.2–0.4 wt.% F and a few Cl.

Oxides

Oxides in Yaojiazhuang complex mainly include magnetite and ilmenite, and the analyses of them are reported in **Supplementary Table 3**.

Except the FeO content of one magnetite from the matrix of pseudoleucite clinopyroxenite is relatively low [81 wt.% with $Fe^{3+}/(Fe^{3+} + Fe^{2+}) = 0.57$], others from both of syenite and clinopyroxenite all exceed 90 wt.% [90.3–93.8 wt.% with $Fe^{3+}/(Fe^{3+} + Fe^{2+}) = 0.65–0.66$]. The TiO_2 content of magnetite varies largely, from 0.3 to 5.2 wt.%, whereas no systematic trend can be found among them. SiO_2 content lies in 0.04–1.3 wt.%. In the TiO_2–FeO–Fe_2O_3 ternary system (**Figure 11E**; Buddington and Lindsley, 1964), magnetite from all lithologies are defined as titanomagnetite.

Ilmenite displays higher TiO_2 content (62.2 wt.%) and lower FeO_{tot} content (28.0 wt.%). In the TiO_2–FeO–Fe_2O_3 ternary system (**Figure 11E**; Buddington and Lindsley, 1964), the ilmenite is yielded as ferropseudobrookite.

Sulfates

Sulfate, i.e., celestine is observed only in the pseudoleucite, and its composition is listed in **Supplementary Table 4**. Celestine contains mainly sulfur and strontium, with SO_3 and SrO contents are 39.76 and 49.92 wt.%. Both of SiO_2 and Al_2O_3 contents are 0.3 wt.%. Celestine contains nearly no F and Cl.

DISCUSSION

Assessment on Alteration

Most syenitic rocks have LOI values less than 1 wt.%, except one syenite (YJZ08-1) and a pegmatitic syenite dyke (YJZ04-1) which are 2.5 and 1.5 wt.%, respectively. The high LOI values for the two samples are mainly attributed to the bound water H_2O^+ and their moisture water contents show no significant differences to other samples (H_2O^- = 0.1–0.4), thus we suggest that the high LOI values are due to a relatively high content of hydrous minerals like analcite and biotite. Similarly, the biotite clinopyroxenite YJZ07-5, clinopyroxenite dyke (YJZ07-2) and K-feldspar clinopyroxenite (YJZ04-4) also show high contents of LOI values up to more than 3 wt.%, whereas their high LOI values are mainly constituted by high bound water up to 2.7 wt.%, consistent with the high contents of biotite and analcite on petrography. The pseudoleucite also has high LOI, high H_2O^+ (3 wt.%) but relatively low H_2O^- (0.5 wt.%), owing to the widespread existing of muscovite, analcite and biotite. Hydrothermal alteration or weathering usually introduce water mobile elements, such as LILE, into rocks, thus the high contents of these elements may indicate the alteration process. However, either on the Sr vs. LOI (**Figure 13A**) or moisture water H_2O^- diagram (**Figure 13B**), no significant correlation is observed for both of clinopyroxenitic or syenitic rocks, implying their primary geochemical signatures are preserved.

There are also classic indices to evaluate the degree of chemical weathering of silicate rocks. For instance, Plagioclase Index of Alteration (PIA) established by Fedo et al. (1995) is widely employed in evaluating the alteration of plagioclase- and/or

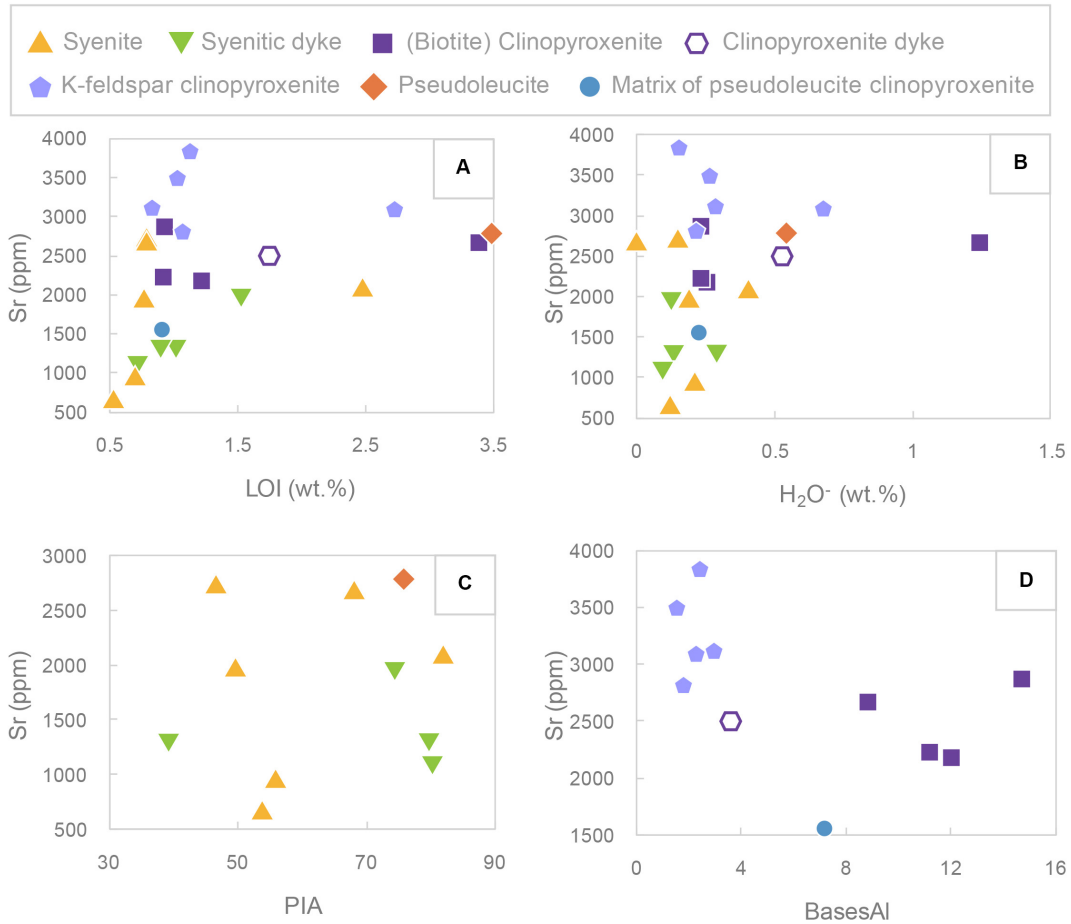

FIGURE 13 | Sr vs. **(A)** LOI (wt.%), **(B)** H_2O^-, **(C)** Plagioclase Index of Alteration (PIA; Fedo et al., 1995) and **(D)** Bases to Alumina ratio (BasesAl; Coleman, 1982) diagrams to evaluate the degree of chemical alteration for Yaojiazhuang samples.

K-feldspar-rich rocks, and Bases to Alumina ratio (BasesAl; Coleman, 1982) is a power tool for mafic rocks. The higher the PIA or the lower the BasesAl, the higher the degree of alteration. There is still no obvious correlation is present for synetic rocks on the Sr vs. PIA diagram (**Figure 13C**) or for clinopyroxenites and K-feldspar clinopyroxenites on the Sr vs. BasesAl diagram (**Figure 13D**). The K-felspar clinopyroxenite with low BasesAl values show higher Sr contents than clinopyroxenites, which shoud be resulted from the higher proportions on Sr-bearing minerals like K-feldspar instead of alteration. Thus, their high Sr contents are able to represent their primary high LILE contents.

Crustal Contamination

Silica saturation index (SSI) was introduced by Motoki et al. (2010) to verify the role of crustal contamination by syenitic magma. The presence of pseudoleucite, nepheline and analcite indicate that the parental magma of Yaojiazhuang complex ought to be peralkaline and undersaturated in silica. The country rocks of the Yaojiazhuang complex is the Archean TTG, which are basically SiO_2-oversaturated and meta- to peraluminous in composition (e.g., Xie et al., 2019; Chen et al., 2020). Since the Yaojiazhuang complex were emplaced into these TTG, it seems unavoidable for the parental magmas were contaminated. Hence, the elevation of SSI is expected due to assimilation of TTG. Meanwhile, such interaction between parental magmas and wall rocks could also decrease the alkali content in the magmas as low-alkali affinity of the TTG (Motoki et al., 2015). Accordingly, on the SSI vs. molar (Na + K)/Al diagram (**Figure 14A**), there are four out of six syenites plotted on the left-top quadrant, implying most of syenites had been largely affected by crustal contamination. This inference is further supported by the plot of SSI vs. $K_2O/(K_2O + Na_2O)$ diagram (**Figure 14B**).

Composition of Parental Magma

As stated above, the clinopyroxenite, K-feldspar clinopyroxenite and syenite exhibit coherent evolution trends both mineralogically and geochemically, indicating these lithologies have a common parental magma. Such inference is also supported by the similar Sr-Nd isotopic compositions of rocks from different lithologies (Chen et al., 2013). Whereas the intrusive contacts between these lithofacies suggest that they are not derived from a single batch of magma.

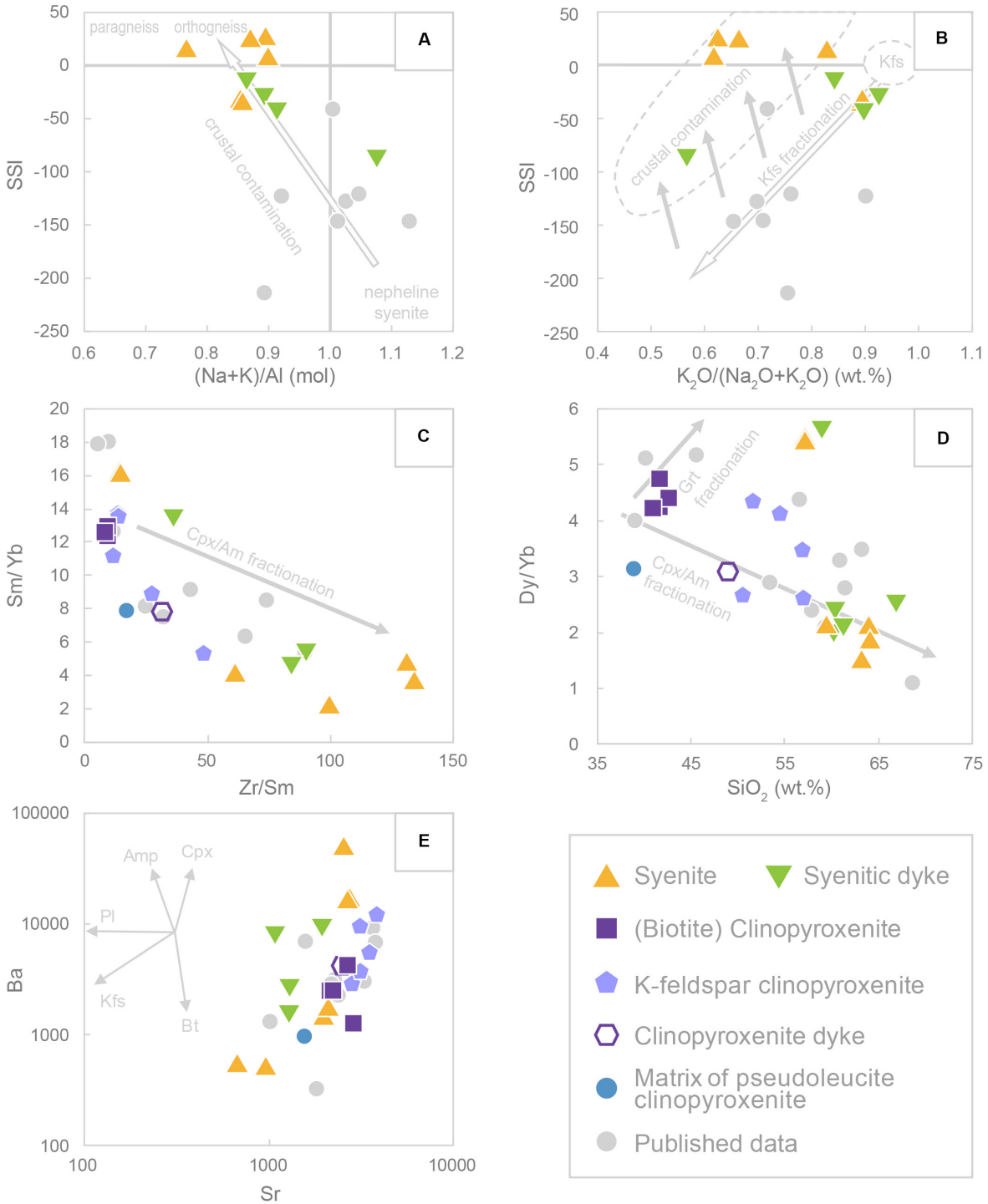

FIGURE 14 | (A,B) Silica saturation index (SSI) vs. (Na + K)/Al (mol.) and $K_2O/(Na_2O + K_2O)$ (wt.%) diagram to discriminate the crustal contamination process (Motoki et al., 2010); **(C)** Sm/Yb vs. Zr/Sm diagram depicting clinopyroxene/amphibole fractionation trend after Xin et al. (2020); **(D)** Dy/Yb vs. SiO_2 diagram illustrating the fractionation of clinopyroxene/amphibole and garnet after Davidson et al. (2007); **(E)** Ba vs. Sr diagram demonstrating the fractionation of various crystals after Xin et al. (2020). Published data are from Chen et al. (2013).

Therefore, it is more likely that there should be a deeper magma chamber where fractional crystallization of parental magma takes place.

Conventionally, the parental magma of Yaojiazhuang complex is thought to be ultrapotassic (Hou, 1990b; Mu and Yan, 1992; Chen et al., 2013), which is defined as $K_2O > 3$ wt.%, MgO > 3

wt.%, and molar $K_2O/Na_2O > 2$ in whole-rock geochemistry according to Foley et al. (1987). While, the MgO contents for all of our syenite samples are below 3 wt.%, and those MgO enriched clinopyroxenite samples contain K_2O less than 3 wt.%. Despite that the molar K_2O/Na_2O in some samples can reach more than 5, there are still some syenite and clinopyroxenite samples having smaller K_2O/Na_2O ratios.

However, the definition in Foley et al. (1987) is based on the whole-rock compositions of sequences of volcanic rocks which are deemed to be liquids. However, rocks from Yaojiazhuang complex are cumulates, the whole-rock composition of which are controlled by the modal proportions of cumulate minerals. Thus, the low MgO K-feldspar-dominated syenites are expected to have low MgO content, and the low K_2O but MgO enriched clinopyroxene dominated clinopyroxenites are expected to be lower in K_2O but higher in MgO. Nevertheless, a feeder dyke (sample YJZ07-2) which is fine-grained and both ultrapotassic in composition (MgO = 6.8 wt.%, K_2O = 7.4 wt.%, molar K_2O/Na_2O = 3.5) could represent the composition of parental magma. Such inference is consistent with abundant presence of K-rich phases including biotite and K-feldspar in the complex. This dyke represents dominant phase among the basic dykes in the studied area and exhibits similar mineralogy and coherent variation trend geochemically with other dominant phases, i.e., clinopyroxenite and syenite. The moderate geochemical characteristics of the clinopyroxenite dyke between clinopyroxenites and K-feldspar clinopyroxenites indicate that clinopyroxenite and K-feldspar clinopyroxenite are derived from the cumulation of mafic minerals, and the syenite is a more evolved phase differentiated from them.

Fractional Crystallization

The bimodal clinopyroxenitic and syenitic series had been speculated to be formed via silicate liquid immiscibility (Hou, 1990b). The magma immiscibility mechanism has also been proposed to explain the petrogenesis of similar bimodal complex like in Hamilton Montana (Lelek, 1979). However, evidence from mineralogy is not consistent with the immiscibility model. For example, equilibrated immiscible Fe- and Si-liquids ought to crystallize same mineral assemblage but with different proportions (e.g., Veksler et al., 2007). According to this criterion, this is not the case for the clinopyroxenite and syenite in Yaojiazhuang as albite is absent in clinopyroxenite and garnet is exclusively seen in the matrix of pseudoleucite clinopyroxenite. Major phase in fractionation crystallization or cumulation can be confirmed by geochemical data plotting. For instance, the Zr/Sm vs. Sm/Yb (**Figure 14C**), Dy/Yb vs. SiO_2 diagram (**Figure 14D**) and Sr vs. Ba diagram (**Figure 14E**) all suggest that a clinopyroxene dominant fractional crystallization/cumulation. Besides, the coupled decrease in Ba and Sr also suggest that the fractionation of K-feldspar plays a dominant role in the differentiation of syenitic rocks, which had also been illustrated by the positively correlation between $K_2O/(K_2O + Na_2O)$ and SSI (**Figure 14B**). Combining the rock and mineral textures as well as geochemical characteristics, the crystallization sequence is inferred as in **Figure 15**, clinopyroxene/apatite/oxides → biotite/titanite → leucite/K-feldspar/analcite/aegirine → albite.

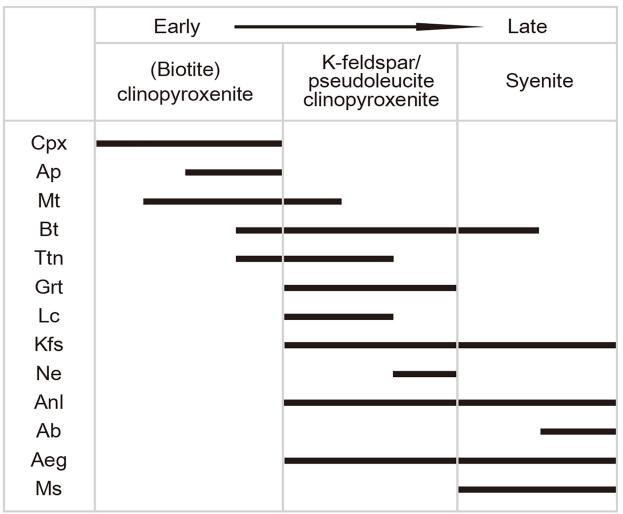

FIGURE 15 | Speculated mineral crystallization sequence of Yaojiazhuang complex.

K-feldspars crystallized as primary phases from the melt including the euhedral crystals in syenite and those interstitial phases in between clinopyroxenes in clinopyroxenite. In addition, some K-feldspar could also be formed by break down of leucite in pseudoleucites. Analcite can be precipitate either as primary mineral in the intergrowths with K-feldspar or secondary phases replacing leucite and/or nepheline.

Fluid-Mineral Interaction

Formation of Pseudoleucite

Pseudoleucite is defined as a result of disintegration of Na-rich leucite into an intergrowth of K-feldspar and nepheline with addition of other mineral phases like muscovite, analcite etc., and it usually occurs as large megacryst in alkaline complexes globally (e.g., Viladkar, 2010). However, its genesis is enigmatic and remains a hotly debated topic (e.g., Knight, 1906; Bowen and Ellestad, 1937; Larsen and Buie, 1938; Barrer and Hinds, 1953; Fudali, 1963; Seki and Kennedy, 1964; Hamilton and McKenzie, 1965; Davidson, 1970; Taylor and MacKenzie, 1975; Gittins et al., 1980). Several genetic models had been proposed including: (1) breakdown of early-formed leucite into K-feldspar and nepheline under subsolidus conditions (T = ∼600°C) during late magmatic stage. (2) reaction of primary leucite with a Na-rich liquid. (3) introduction of Na^+ from hydrous glass or aqueous vapor by ion exchange. Here, we will briefly discuss these theories as the possible mechanism to produce the pseudoleucites in Yaojiazhuang complex.

Conventionally, problem arises to the subsolidus breakdown of leucite because although experiments shows that leucite could accommodate about 40 wt.% $NaAlSi_2O_6$ in the solid solution (Taylor and MacKenzie, 1975), natural leucite has never been observed to contain excess amount of Na to form the intergrowth with sodium-bearing phases on decomposition

(Viladkar, 2010). The abundant sodium-rich phase like nepheline and analcite in the mineralogy of the pseudoleucite suggest they are generated from a pre-existing Na-rich phase. Therefore, the pseudoleucite in Yaojiazhuang samples cannot be explained by subsolidus break down of potassic leucite alone, but processes introducing sodium into leucite to form a metastable sodic leucite prior to breakdown seem to be necessary (Taylor and MacKenzie, 1975).

Reaction between leucite and Na-rich melt/liquid was proposed as mechanism to produce a nepheline-K-feldspar pseudomorph and former leucite disappears (Bowen and Ellestad, 1937; Edgar, 1984). An outstanding feature of this theory is that, the leucite crystal morphology can hardly be well preserved during the reaction with melt/liquid (Taylor and MacKenzie, 1975). We observed in our samples, the pseudoleucite generally exhibit the pentagonal icositetrahedron morphology of leucite in macro scale, whereas many of their rims are curved and modified in micro scale, suggesting that such a reaction process cannot be totally ignored (**Figure 4**). Indeed, the pseudoleucite is considered as a late-stage phase after mafic minerals due to these vermicular nepheline-feldspar or analcite-feldspar intergrowths are also present as anhedral interstices in the matrix or clinopyroxenites. The Na content in zoned clinopyroxenes are also observed progressively increase from core to rim, supporting to an increasingly sodic crystal mush in the late stage. Moreover, various minor mineral phases (e.g., biotite, clinopyroxene, apatite, titanite) occur within the pseudoleucite and show no obvious compositional differences to those in the matrix, suggesting they are appeared to be primary magmatic inclusions. These phases introduce additional elements into the pseudoleucites, which advises investigations only based in traditional petrogeny's residua system (SiO_2–$NaAlSiO_4$–$KAlSiO_4$, quartz-nepheline-kalsilite) is not enough (Edgar, 1984).

Alkali ion exchange reaction is a reaction of pre-existing potassic leucite and sodic glass and/or aqueous vapor by cation substitution under subsolidus conditions, resulting soda leucite and later exsolution without modification of previous crystal morphology (Taylor and MacKenzie, 1975). However, this mechanism seems not to be the case for Yaojiazhuang samples, because our pseudoleucites generally have K-feldspar rims but nepheline-feldspar cores (**Figure 4E**), which means the bulk composition in the cores are much richer in Na than the rims. Nevertheless, the presence of a magmatic sodium rich fluid could be possible. Amphibole hygrometer suggests water content of melt during late-stage evolution exceeds 3 wt.%, therefore leucites are possible to start nucleation at the late stage of crystallization when the cooling rate is expected to be speed up at hydrous undercooling condition, and form the crystal skeletons (rims) resemble those rapid-grow hollow textures (Faure et al., 2003). While, following the formation of anhydrous rims, further crystallization of cores is tend to be impeded due to the increase of water activity and the residue melt compositionally equals to nepheline + K-feldspar. With a rapid degassing, the final liquid crystallizes a vermicular and fingerprinted intergrowth of cotectic nepheline and K-feldspar (Gittins et al., 1980). The leucite skeletons may latterly be transformed to K-feldspar and nepheline or react to form analcite in the presence of exsolved fluids (Henderson and Gibb, 1977; Wilkinson and Hensel, 1994). The exsolved fluid by degassing may also result in the coarsening of some nephelines (**Figure 4F**) by self-alteration (Ballhaus et al., 2015), and introduce other hydrophilic elements such as Ca into nephelines to form cancrinite before subsequent weathered to kaolin. Complementary evidences for the activity of magmatic sodium-rich fluids during the late-stage magmatic evolution are the transformation of initial leucite to analcite in the matrix (**Figure 5F**), the widespread albite lamellae in K-feldspars and the pegmatitic syenites at the top of the intrusion (**Figure 2E**). In summary, the presence of pseudoleucite and hydrous primary minerals provided solid evidences for the activities of fluids. Fluids saturation and exsolution may have been achieved during decompression of replenished magmas from deep and during crystallization of anhydrous minerals like clinopyroxene.

Implications for the Formation of the Apatite and IOA Ores

The widespread interstitial biotite in clinopyroxenite and presence of glimmerite imply that the late-stage melt could be significantly hydrous. Dissolved aqueous fluid could be over-saturated at some point and exsolved from the crystallizing magma during decompression (e.g., Moore et al., 1998; Dixon et al., 1995; Newman and Lowenstern, 2002; Ballhaus et al., 2015) or during isobaric crystallization of anhydrous minerals (Candela, 1997), such as clinopyroxene and leucite in this study. Moreover, the presence of magmatic calcite also indicates that the parental magma could also be CO_2-rich (Mu et al., 1999), which suppresses the H_2O solubility in melt, resulting in exsolution of H_2O at a relatively lower concentration (Caricchi et al., 2018; Edmonds and Woods, 2018). Hence, in the case of Yaojiazhuang, the scenario involving exsolution of aqueous fluids during the magmatic stage is expected. Besides, these aqueous fluids should also be abundant in F, due to F-rich biotite is widespread throughout the complex.

Experimental studies indicate that phosphate saturation in silicate melts is mainly controlled by SiO_2 and CaO, and addition of H_2O and/or F in silicate magmas leads to saturation of apatite (Tollari et al., 2006, 2008). The Yaojiazhuang complex is characterized by relatively high CaO and low SiO_2 content. Hence, it is thus expected that the magmatic liquids during the differentiation of the complex may reach high concentrations in both Fe and P. Once the concentration of H_2O and/or F was elevated by fractionation or other processes, saturation of apatite will be reached. Magnetite will also crystallize induced by decrease in P concentration in the melt (Tollari et al., 2006), rather than elevation of oxygen fugacity during the late stage of differentiation. In other words, apatite and magnetite preferentially co-crystallized from the magmas. Besides, the exsolution of aqueous fluids is considered as a potential mechanism in the formation of porphyritic or spheroidal structure rocks hosting economic ore deposits (Huber et al., 2012; Ballhaus et al., 2015; Guo and Audétat, 2017). As described above,

the IOA ores occurred as rocks with spheroidal structure in the field. Therefore, we propose that the fluids exsolution could also be a viable mechanism to concentrate not only magnetite but also apatite by wetting (Ballhaus et al., 2015) and formed the apatite and IOA ore in Yaojiazhuang complex. Notably, Knipping et al. (2015a; 2015b) have already advocated that flotation, coalescence and transport of magnetite-bubble pairs within a magma chamber is the key process for the formation of IOA ores. However, their model has only focused on enrichment of iron oxide instead of iron oxide plus apatite, i.e., IOA ores. Nevertheless, we admit that indeed, the role of exsolved fluids could be more important than we thought. Hence, if this is the case, the occurrence of apatite and IOA ores in Yaojiazhuang provides direct petrologic evidence for such a model involving fluids exsolution and concentration of iron oxide and apatite.

CONCLUSION

(1) The bimodal lithologies are more likely to be formed via crystallization fractionation of an ultrapotassic parental magma instead of silicate liquid immiscibility. Fractionations of both clinopyroxene and K-feldspar, and repeated magma replenishment in the crustal chamber played an important role during the differentiation of primitive ultrapotassic magmas. Crustal contamination may also had been involved during the solidification of the complex. Except that, during the emplacement of Yaojiazhuang magma, decompression, fractionation of anhydrous clinopyroxene and the enhancement by CO_2 may result in the exsolution of an aqueous fluid.

(2) The genesis of pseudoleucite is related to original leucite crystallization from an evolved, silica-undersaturated magma followed by the interaction with sodium-rich fluids during the late-magmatic stage. Transportation of aqueous fluid within crystal mush is believed to be a key factor in generating the leucite pseudomorph with ambiguous crystal boundary.

(3) The differentiation under fluid-rich condition in the crust could be responsible for the petrogenesis of Yaojiazhuang ultrapotassic complex, thus the concentration of apatite and IOA ores is presumed to be closely related to the fluid exsolution process as well.

DATA AVAILABILITY STATEMENT

The original contributions presented in this study are included in the article/**Supplementary Material**, further inquiries can be directed to the corresponding authors.

AUTHOR CONTRIBUTIONS

TH and RP designed the research, conducted the field trip, and all the analysis works together. Following data treatment were undertaken by RP and TH. All authors actively participated in the subsequent discussions and interpretation of the data as well as in the preparation of the manuscript.

FUNDING

This work was supported by the National Natural Science Foundation of China (41922012, 91962102, and 41761134086) and 2016YFC0600502, MOST Special Fund from the State Key Laboratory of Geological Processes and Mineral Resources, China University of Geosciences (MSFGPMR201804), and 111 Project (B18048). This work also builds partly on research funded by the Sino-German NSFC-DFG project (DFG, HO1337/39-1).

ACKNOWLEDGMENTS

We are grateful to editor DL and two reviewers, WC and JZ for their constructive and helpful comments. We also thank Jihao Zhu at Key Laboratory of Submarine Geosciences, State Oceanic Administration, Second Institute of Oceanography, Ministry of Natural Resources for support in the use of SEM and EMPA, and Qiuyun Yuan at Nanjing Hongchuang Exploration Technology Service Co., Ltd. for help in sample processes. Diao Luo and Xudong Wang are thanked for their help in the field.

SUPPLEMENTARY MATERIAL

The Supplementary Material for this article can be found online at: https://www.frontiersin.org/articles/10.3389/feart.2020.00357/full#supplementary-material

REFERENCES

Ballhaus, C., Fonseca, R. O., Münker, C., Kirchenbaur, M., and Zirner, A. (2015). Spheroidal textures in igneous rocks–Textural consequences of H2O saturation in basaltic melts. *Geochim. Cosmochim. Acta* 167, 241–252. doi: 10.1016/j.gca.2015.07.029

Barrer, R. M., and Hinds, L. (1953). Ion-exchange in crystals of analcite and leucite. *J. Chem. Soc.* 386, 1879–1888.

Bodeving, S., Williams-Jones, A. E., and Swinden, S. (2017). Carbonate–silicate melt immiscibility, REE mineralising fluids, and the evolution of the Lofdal Intrusive Suite, Namibia. *Lithos* 268, 383–398. doi: 10.1016/j.lithos.2016.11.024

Bowen, N. L., and Ellestad, R. B. (1937). Leucite and pseudoleucite. *Am. Mineral. J. Earth Planet. Mater.* 22, 409–415.

Brenna, M., Nakada, S., Miura, D., Toshida, K., Ito, H., Hokanishi, N., et al. (2015). A trachyte–syenite core within a basaltic nest: filtering of primitive injections by a multi-stage magma plumbing system (Oki-Dôzen, south-west Japan). *Contrib. Mineral. Petrol.* 170:22. doi: 10.1007/s00410-015-1181-0

Buddington, A. F., and Lindsley, D. H. (1964). Iron-titanium oxide minerals and synthetic equivalents. *J. Petrol.* 5, 310–357. doi: 10.1093/petrology/5.2.310

Burchardt, S. (2018). *Volcanic and Igneous Plumbing Systems: Understanding Magma Transport, Storage, and Evolution in the Earth's Crust*. Amsterdam: Elsevier.

Candela, P. A. (1997). A review of shallow, ore-related granites: textures, volatiles, and ore metals. *J. Petrol.* 38, 1619–1633. doi: 10.1093/petroj/38.12.1619

Caricchi, L., Sheldrake, T. E., and Blundy, J. (2018). Modulation of magmatic processes by CO2 flushing. *Earth Planet. Sci. Lett.* 491, 160–171. doi: 10.1016/j.epsl.2018.03.042

Chen, B., Niu, X., Wang, Z., Gao, L., and Wang, C. (2013). Geochronology, petrology, and geochemistry of the Yaojiazhuang ultramafic-syenitic complex from the North China Craton. *Sci. China Earth Sci.* 56, 1294–1307. doi: 10.1007/s11430-013-4603-8

Chen, Y., Zhang, J., Liu, J., Han, Y., Yin, C., Qian, J., et al. (2020). Crustal growth and reworking of the eastern North China Craton: constraints from the age and geochemistry of the Neoarchean Taishan TTG gneisses. *Precambrian Res.* 343:105706. doi: 10.1016/j.precamres.2020.105706

Cheng, C., and Sun, S. (2003). The Fanshan apatite-magnetite deposit in the potassic ultramafic layered intrusion, north China. *Resour. Geol.* 53, 163–174. doi: 10.1111/j.1751-3928.2003.tb00167.x

Coleman, R. G., Lee, D. E., Beatty, L. B., and Brannock, W. W. (1965). Eclogites and Eclogites: their differences and similarities. *GSA Bull.* 76, 483–508.

Coleman, S. M. (1982). Chemical weathering of basalts and andesites: evidence from weathering rinds. *Geol. Surv. Prof. Pap.* 1246:51. doi: 10.3133/pp1246

Comin-Chiaramonti, P., Cundari, A., Ruberti, E., De Min, A., Gittins, J., Gomes, C. B., et al. (2009). Genesis of analcime and nepheline-potassium feldspar-kalsilite intergrowths: a review. *Acta Vulcanol.* 20, 81–90.

Conticelli, S., Avanzinelli, R., Poli, G., Braschi, E., and Giordano, G. (2013). Shift from lamproite-like to leucititic rocks: Sr–Nd–Pb isotope data from the Monte Cimino volcanic complex vs. the Vico stratovolcano, Central Italy. *Chem. Geol.* 353, 246–266. doi: 10.1016/j.chemgeo.2012.10.018

Conticelli, S., Carlson, R. W., Widom, E., and Serri, G. (2007). Chemical and isotopic composition (Os, Pb, Nd, and Sr) ofNeogene to Quaternary calc-alkalic, shoshonitic, and ultrapotassic ma?c rocks from the Italian peninsula: inferences on the nature of their mantle sources. *Spec. Pap. Geol. Soc. Am.* 418, 171–202. doi: 10.1130/2007.2418(09)

Conticelli, S., Guarnieri, L., Farinelli, A., Mattei, M., Avanzinelli, R., Bianchini, G., et al. (2009). Trace elements and Sr–Nd–Pb isotopes of K-rich, shoshonitic, and calc-alkaline magmatism of the Western Mediterranean Region: genesis of ultrapotassic to calc-alkaline magmatic associations in a post-collisional geodynamic setting. *Lithos* 107, 68–92. doi: 10.1016/j.lithos.2008.07.016

Conticelli, S., and Peccerillo, A. (1992). Petrology and geochemistry of potassic and ultrapotassic volcanism in central Italy: petrogenesis and inferences on the evolution of the mantle sources. *Lithos* 28, 221–240. doi: 10.1016/0024-4937(92)90008-M

Davidson, A. (1970). Nepheline-K-feldspar intergrowth from Kaminak Lake, Northwest territories. *Can. Mineral.* 10, 191–206.

Davidson, J., Turner, S., Handley, H., Macpherson, C., and Dosseto, A. (2007). Amphibole "sponge" in arc crust? *Geology* 35, 787–790. doi: 10.1130/G23637A.1

Dawson, J. B. (1987). The kimberlite clan: relationship with olivine and leucite lamproites, and inferences for upper-mantle metasomatism. *Geol. Soc. Lond. Spec. Publ.* 30, 95–101. doi: 10.1144/GSL.SP.1987.030.01.07

Dixon, J. E., Stolper, E. M., and Holloway, J. R. (1995). An experimental study of water and carbon dioxide solubilities in mid-ocean ridge basaltic liquids. Part I: calibration and solubility models. *J. Petrol.* 36, 1607–1631. doi: 10.1093/oxfordjournals.petrology.a037267

Edgar, A. D. (1984). "Chemistry, occurrence and paragenesis of feldspathoids: a review," in *Feldspars and Feldspathoids*, ed. W. L. Brown (Dordrecht: Springer), 501–532. doi: 10.1007/978-94-015-6929-3_14

Edmonds, M., and Woods, A. W. (2018). Exsolved volatiles in magma reservoirs. *J. Volcanol. Geotherm. Res.* 368, 13–30. doi: 10.1016/j.jvolgeores.2018.10.018

Faure, F., Trolliard, G., Nicollet, C., and Montel, J. M. (2003). A developmental model of olivine morphology as a function of the cooling rate and the degree of undercooling. *Contrib. Mineral. Petrol.* 145, 251–263. doi: 10.1007/s00410-003-0449-y

Fedo, C. M., Nesbitt, H. W., and Young, G. M. (1995). Unraveling the effects of potassium metasomatism in sedimentary rocks and paleosols, with implications for paleoweathering conditions and provenance. *Geology* 23, 921–924.

Ferlito, C., and Lanzafame, G. (2010). The role of supercritical fluids in the potassium enrichment of magmas at Mount Etna volcano (Italy). *Lithos* 119, 642–650. doi: 10.1016/j.lithos.2010.08.006

Foley, S., and Peccerillo, A. (1992). Potassic and ultrapotassic magmas and their origin. *Lithos* 28, 181–185. doi: 10.1016/0024-4937(92)90005-J

Foley, S., Venturelli, G., Green, D. H., and Toscani, L. (1987). The ultrapotassic rocks: characteristics, classification, and constraints for petrogenetic models. *Earth Sci. Rev.* 24, 81–134. doi: 10.1016/0012-8252(87)90001-8

Fudali, R. F. (1963). Experimental studies bearing on the origin of pseudoleucite and associated problems of alkalic rock systems. *Geol. Soc. Am. Bull.* 74, 1101–1126.

Gaeta, M., Freda, C., Marra, F., Arienzo, I., Gozzi, F., Jicha, B., et al. (2016). Paleozoic metasomatism at the origin of Mediterranean ultrapotassic magmas: constraints from time-dependent geochemistry of Colli Albani volcanic products (Central Italy). *Lithos* 244, 151–164. doi: 10.1016/j.lithos.2015.11.034

Gittins, J., Fawcett, J. J., Brooks, C. K., and Rucklidge, J. C. (1980). Intergrowths of nepheline-potassium feldspar and kalsilite-potassium feldspar: a re-examination of the 'pseudo-leucite problem'. *Contrib. Mineral. Petrol.* 73, 119–126. doi: 10.1007/BF00371386

Guo, H., and Audétat, A. (2017). Transfer of volatiles and metals from mafic to felsic magmas in composite magma chambers: an experimental study. *Geochim. Cosmochim. Acta* 198, 360–378. doi: 10.1016/j.gca.2016.11.029

Hamilton, D. L., and McKenzie, W. (1965). Phase equilibria studies in the system NaAlSiO4 (nepheline)-KAlSiO4 (kalsilite)-SiO2 (quartz). *Mineral. Magaz.* 69, 134–214. doi: 10.1180/minmag.1965.034.268.17

Henderson, C. M. B., and Gibb, F. G. F. (1977). Formation of analcime in the Dippin Sill, Isle of Arran. *Mineral. Magaz.* 41, 534–537. doi: 10.1180/minmag.1977.041.320.21

Hou, T., Zhang, Z., Keiding, J. K., and Veksler, I. V. (2015). Petrogenesis of the ultrapotassic fanshan intrusion in the North China craton: implications for lithospheric mantle metasomatism and the origin of apatite ores. *J. Petrol.* 56, 893–918. doi: 10.1093/petrology/egv021

Hou, Z. Q. (1990a). Silicate liquid immiscibility of the Yangyuan-Fanshan complex in Hebei province and the origin of the Fanshan type phosphorus deposits. *Miner. Deposits* 9, 119–128. doi: 10.16111/j.0258-7106.1990.02.003

Hou, Z. Q. (1990b). The pyroxenite-syenite suite of yangyuan complex in hebei province and silicate liquid immiscibility. *Geoscience* 4, 53–64.

Huber, C., Bachmann, O., Vigneresse, J. L., Dufek, J., and Parmigiani, A. (2012). A physical model for metal extraction and transport in shallow magmatic systems. *Geochem. Geophys. Geosyst.* 13:Q08003. doi: 10.1029/2012GC004042

Ihlen, P. M., Schiellerup, H., Gautneb, H., and Skår, Ø (2014). Characterization of apatite resources in Norway and their REE potential — A review. *Ore Geol. Rev.* 58, 126–147. doi: 10.1016/j.oregeorev.2013.11.003

Jeffery, A. J., Gertisser, R., Troll, V. R., Jolis, E. M., Dahren, B., Harris, C., et al. (2013). The pre-eruptive magma plumbing system of the 2007–2008 dome-forming eruption of Kelut volcano, East Java, Indonesia. *Contrib. Mineral. Petrol.* 166, 275–308. doi: 10.1007/s00410-013-0875-4

Jiang, N., Chu, X., Mizuta, T., Ishiyama, D., and Mi, J. (2004). A magnetite-apatite deposit in the Fanshan alkaline ultramafic complex, northern China. *Econ. Geol.* 99, 397–408. doi: 10.2113/gsecongeo.99.2.397

Knight, C. W. (1906). A new occurrence of pseudo-leucite. *Am. J. Sci.* 21, 286–293. doi: 10.2475/ajs.s4-21.124.286

Knipping, J., Webster, J. D., Simon, A. C., and Holtz, F. (2019). Accumulation of magnetite by flotation on bubbles during decompression of silicate magma. *Sci. Rep.* 9:3852. doi: 10.1038/s41598-019-40376-1

Knipping, J. L., Bilenker, L. D., Simon, A. C., Reich, M., Barra, F., Deditius, A. P., et al. (2015a). Giant Kiruna-type deposits form by efficient flotation of magmatic magnetite suspensions. *Geology* 43, 591–594. doi: 10.1130/G36650.1

Knipping, J. L., Bilenker, L. D., Simon, A. C., Reich, M., Barra, F., Deditius, A. P., et al. (2015b). Trace elements in magnetite from massive iron oxide-apatite deposits indicate a combined formation by igneous and magmatic-hydrothermal processes. *Geochim. Cosmochim. Acta* 171, 15–38. doi: 10.1016/j.gca.2015.08.010

Kogarko, L. (2018). Chemical composition and petrogenetic implications of apatite in the Khibiny apatite-nepheline deposits (Kola Peninsula). *Minerals* 8:532. doi: 10.3390/min8110532

Kolker, A. (1982). Mineralogy and geochemistry of Fe-Ti oxide and apatite (nelsonite) deposits and evaluation of the liquid immiscibility hypothesis. *Econ. Geol.* 77, 1146–1158. doi: 10.2113/gsecongeo.77.5.1146

La Cruz, N. L., Simon, A. C., Wolf, A. S., Reich, M., Barra, F., and Gagnon, J. E. (2019). The geochemistry of apatite from the Los Colorados iron oxide–apatite deposit, Chile: implications for ore genesis. *Miner. Depos.* 54, 1143–1156. doi: 10.1007/s00126-019-00861-z

Larsen, E. S., and Buie, B. F. (1938). Potash analcime and pseudoleucite from the Highwood Mountains of Montana. *Am. Mineral. J. Earth Planet. Mater.* 23, 837–849.

Lelek, J. J. (1979). *The Skalkaho Pyroxenite-Syenite Complex East of Hamilton Montana and the Role of Magma Immiscibility in its Formation*. Graduate Student Theses, Dissertations, & Professional Papers, The University of Montana, Missoula, MT.

Liu, D. Y., Nutman, A. P., Compston, W., Wu, J. S., and Shen, Q. H. (1992). Remnants of =3800 Ma crust in the Chinese part of the Sino-Korean craton. *Geology* 20, 339–342.

Liu, X., and Tang, Y. (2018). The characteristics and implication of the zonation in clinopyroxene phenocrysts from the Yaojiazhuang ultramafic-syenitic complex, northwestern Hebei Province. *Acta Petrol. Sin.* 34, 3315–3326.

Lobach-Zhuchenko, S. B., Rollinson, H., Chekulaev, V. P., Savatenkov, V. M., Kovalenko, A. V., Martin, H., et al. (2008). Petrology of a Late Archaean, highly potassic, sanukitoid pluton from the Baltic Shield: insights into Late Archaean mantle metasomatism. *J. Petrol.* 49, 393–420. doi: 10.1093/petrology/egm084

Ma, H., Hu, Y., and Fang, T. (1999). TWOLIQ.FOR: a FORTRAN77 program for simulating immiscibility in silicate liquids. *Comput. Geosci.* 25, 151–159. doi: 10.1016/S0098-3004(98)00115-0

Marks, M. A., Schilling, J., Coulson, I. M., Wenzel, T., and Markl, G. (2008). The alkaline–peralkaline Tamazeght complex, High Atlas Mountains, Morocco: mineral chemistry and petrological constraints for derivation from a compositionally heterogeneous mantle source. *J. Petrol.* 49, 1097–1131. doi: 10.1093/petrology/egn019

Miller, C. H., Schuster, R., Klötzli, U., Frank, W., and Purtscheller, F. (1999). Post-collisional potassic and ultrapotassic magmatism in SW Tibet: geochemical and Sr–Nd–Pb–O isotopic constraints for mantle source characteristics and petrogenesis. *J. Petrol.* 40, 1399–1424. doi: 10.1093/petroj/40.9.1399

Mokhtari, M. A. A., Zadeh, G. H., and Emami, M. H. (2013). Genesis of iron-apatite ores in Posht-e-Badam Block (Central Iran) using REE geochemistry. *J. Earth Syst. Sci.* 122, 795–807. doi: 10.1007/s12040-013-0313-z

Moore, G., Vennemann, T., and Carmichael, I. S. E. (1998). An empirical model for the solubility of H2O in magmas to 3 kilobars. *Am. Mineral.* 83, 36–42. doi: 10.2138/am-1998-1-203

Motoki, A., Sichel, S. E., Vargas, T., Aires, J. R., Iwanuch, W., Mello, S. L. M., et al. (2010). *Geochemical evolution of the felsic alkaline rocks of Tanguá and Rio Bonito intrusive bodies, State of Rio de Janeiro, Brazil*. São Paulo: UNESP, 291–310.

Motoki, A., Sichel, S. E., Vargas, T., Melo, D. P., and Motoki, K. F. (2015). Geochemical behaviour of trace elements during fractional crystallization and crustal assimilation of the felsic alkaline magmas of the state of Rio de Janeiro, Brazil. *Anais Acad. Bras. Ciencias* 87, 1959–1979. doi: 10.1590/0001-3765201520130385

Mu, B., Shao, J., and Bian, Z. (1999). Discovery of carbonatite in the Fanshan alkaline igneous complex in Hebei province, China. *Acta Scientiarum Naturalium Universitatis Pekinensis* 35, 243–247.

Mu, B., and Yan, G. (1992). Geochemistry of Triassic alkaline or subalkaline igneous complexes in the Yan-Liao area and their significance. *Acta Geol. Sin.* 66, 108–121.

Newman, S., and Lowenstern, J. B. (2002). VolatileCalc: a silicate melt–H2O–CO2 solution model written in Visual Basic for excel. *Comput. Geosci.* 28, 597–604. doi: 10.1016/S0098-3004(01)00081-4

Nikolenko, A. M., Redina, A. A., Doroshkevich, A. G., Prokopyev, I. R., Ragozin, A. L., and Vladykin, N. V. (2018). The origin of magnetite-apatite rocks of Mushgai-Khudag Complex, South Mongolia: mineral chemistry and studies of melt and fluid inclusions. *Lithos* 320, 567–582. doi: 10.1016/j.lithos.2018.08.030

Notholt, A. J. (1979). The economic geology and development of igneous phosphate deposits in Europe and the USSR. *Econ. Geol.* 74, 339–350. doi: 10.2113/gsecongeo.74.2.339

Ren, R., Han, B.-F., Zhang, L., and Chen, J. F. (2009). Zircon SHRIMP U-Pb dating of the Fanshan potassic alkaline ultramafite-syenite complex in Hebei Province, China. *Acta Petrol. Sin.* 25, 588–594.

Roedder, E. (1992). Fluid inclusion evidence for immiscibility in magmatic differentiation. *Geochim. Cosmochim. Acta* 56, 5–20. doi: 10.1016/0016-7037(92)90113-W

Rogers, N. W., De Mulder, M., and Hawkesworth, C. J. (1992). An enriched mantle source for potassic basanites: evidence from Karisimbi volcano, Virunga volcanic province, Rwanda. *Contrib. Mineral. Petrol.* 111, 543–556. doi: 10.1007/BF00320908

Seki, Y., and Kennedy, G. C. (1964). The breakdown of potassium feldspar, KAlSi3O8 at high temperatures and high pressures. *Am. Mineral. J. Earth Planet. Mater.* 49, 1688–1706.

Soder, C. G., and Romer, R. L. (2018). Post-collisional potassic–ultrapotassic magmatism of the Variscan Orogen: implications for mantle metasomatism during continental subduction. *J. Petrol.* 59, 1007–1034. doi: 10.1093/petrology/egy053

Sokół, K., Halama, R., Meliksetian, K., Savov, I. P., Navasardyan, G., and Sudo, M. (2018). Alkaline magmas in zones of continental convergence: the Tezhsar volcano-intrusive ring complex, Armenia. *Lithos* 320, 172–191. doi: 10.1016/j.lithos.2018.08.028

Sun, S. S., and McDonough, W. F. (1989). Chemical and isotopic systematics of oceanic basalts: implications for mantle composition and processes. *Geol. Soc. Lond. Spec. Public.* 42, 313–345. doi: 10.1144/GSL.SP.1989.042.01.19

Sun, Y., Ying, J., Zhou, X., Chu, Z., and Su, B. (2014). Geochemistry of ultrapotassic volcanic rocks in Xiaogulihe NE China: implications for the role of ancient subducted sediments. *Lithos* 208, 53–66. doi: 10.1016/j.lithos.2014.08.026

Tacker, R. C., and Stormer, J. C. (1989). A thermodynamic model for apatite solid solutions, applicable to high-temperature geologic problems. *Am. Mineral.* 74, 877–888.

Tang, Y., Zhang, H., and Ying, J. (2014). Genetic significance of Triassic alkali-rich intrusive rocks in the Yinshan and neighboring areas. *Acta Petrol. Sin.* 30, 2031–2040.

Taylor, D., and MacKenzie, W. S. (1975). A contribution to the pseudoleucite problem. *Contrib. Mineral. Petrol.* 49, 321–333. doi: 10.1007/BF00376184

Thompson, R. N., Leat, P. T., Dickin, A. P., Morrison, M. A., Hendry, G. L., and Gibson, S. A. (1990). Strongly potassic mafic magmas from lithospheric mantle sources during continental extension and heating: evidence from Miocene minettes of northwest Colorado, USA. *Earth Planet. Sci. Lett.* 98, 139–153. doi: 10.1016/0012-821X(90)90055-3

Tollari, N., Barnes, S. J., Cox, R. A., and Nabil, H. (2008). Trace element concentrations in apatites from the Sept-Îles Intrusive Suite, Canada—implications for the genesis of nelsonites. *Chem. Geol.* 252, 180–190. doi: 10.1016/j.chemgeo.2008.02.016

Tollari, N., Toplis, M. J., and Barnes, S. J. (2006). Predicting phosphate saturation in silicate magmas: an experimental study of the effects of melt composition and temperature. *Geochim. Cosmochim. Acta* 70, 1518–1536. doi: 10.1016/j.gca.2005.11.024

Veksler, I. V., Dorfman, A. M., Borisov, A. A., Wirth, R., and Dingwell, D. B. (2007). Liquid immiscibility and evolution of basaltic magma. *J. Petrol.* 48, 2187–2210. doi: 10.1093/petrology/egm056

Viladkar, S. G. (2010). The origin of pseudoleucite in tinguaite, Ghori, India: a re-evaluation. *Petrology* 18, 544–554. doi: 10.1134/S0869591110050061

Wilkinson, J. F. G., and Hensel, H. D. (1994). Nephelines and analcimes in some alkaline igneous rocks. *Contrib. Mineral. Petrol.* 118, 79–91. doi: 10.1007/BF00310612

Wolff, J. A. (2017). On the syenite-trachyte problem. *Geology* 45, 1067–1070. doi: 10.1130/G39415.1

Xiao, W., Windley, B. F., Hao, J., and Zhai, M. (2003). Accretion leading to collision and the Permian Solonker suture, Inner Mongolia, China: termination of the central Asian orogenic belt. *Tectonics* 22:1069. doi: 10.1029/2002TC001484

Xie, H., Wan, Y., Dong, C., Kröner, A., Xie, S., Liu, S., et al. (2019). Late Neoarchean synchronous TTG gneisses and potassic granitoids in southwestern Liaoning Province, North China Craton: Zircon U-Pb-Hf isotopes, geochemistry and tectonic implications. *Gondwana Res.* 70, 171–200. doi: 10.1016/j.gr.2018.11.016

Xin, W., Sun, F. Y., Xu, Z. H., Lu, Y. H., Zhang, Y. J., Deng, J. F., et al. (2020). Potassic/ultrapotassic intrusions at the southwestern margin of the Yangtze Craton, southwestern China: petrogenesis and implications for the metal and fluid source of non-arc porphyry Cu–(Mo–Au) deposits. *Lithos* 352:105294. doi: 10.1016/j.lithos.2019.105294

Zhang, M., Suddaby, P., Thompson, R. N., Thirlwall, M. F., and Menzies, M. A. (1995). Potassic volcanic rocks in NE China: geochemical constraints on mantle

source and magma genesis. *J. Petrol.* 36, 1275–1303. doi: 10.1093/petrology/36.5.1275

Zhang, S., Zhao, Y., Song, B., Hu, J. M., Liu, S. W., Yang, Y. H., et al. (2009). Contrasting Late Carboniferous and Late Permian-Middle Triassic intrusive suites from the northern margin of the North China craton: geochronology, petrogenesis, and tectonic implications. *Geol. Soc. Am. Bull.* 121, 181–200. doi: 10.1130/B26157.1

Zhang, S., Zhao, Y., Ye, H., Hou, K., and Li, C. (2012). Early Mesozoic alkaline complexes in the northern North China Craton: implications for cratonic lithospheric destruction. *Lithos* 155, 1–18. doi: 10.1016/j.lithos.2012.08.009

Zhang, Z. (1999). Rock associations and petrogenesis of Indosinian Alkaline complex of the north Hebei province, north China. *Sci. Geol. Sin.* 8, 65–76.

Zhang, Z., and Wang, Y. (1997). Indosinian alkaline magmatism in north Hebei province and its geodynamic significance. *Bull. Mineral. Petrol. Geochem.* 16, 214–217.

Zhao, G., Cawood, P. A., Wilde, S. A., and Lu, L. (2001). High-pressure granulites (retrograded eclogites) from the hengshan complex, North China craton: petrology and tectonic implications. *J. Petrol.* 42, 1141–1170. doi: 10.1093/petrology/42.6.1141

Zhao, G., Wilde, S. A., Sun, M., Guo, J., Kroner, A., Li, S., et al. (2008). SHRIMP U-Pb zircon geochronology of the huai'an complex: constraints on late archean to paleoproterozoic magmatic and metamorphic events in the trans-north china orogen. *Am. J. Sci.* 308, 270–303. doi: 10.2475/03.2008.04

Conflict of Interest: The authors declare that the research was conducted in the absence of any commercial or financial relationships that could be construed as a potential conflict of interest.